Slovak University of Technology in Bratislava
Faculty of Civil Engineering

Ing. Richard Czikhardt

Executive summary of the dissertation thesis

InSAR Measurements in a Geodetic Reference Frame

to acquire the academic degree philosophiae doctor, PhD.

in the doctoral study programme 3636 geodesy and cartography

in the full-time form of study.

Bratislava, 31. May 2021

The dissertation thesis was prepared at the Department of Theoretical Geodesy and Geoinformatics, Faculty of Civil Engineering, Slovak University of Technology in Bratislava.

PhD. student: Ing. Richard Czikhardt
Department of Theoretical Geodesy and Geoinformatics
faculty of Civil Engineering, STU in Bratislava
Radlinského 11, 810 05 Bratislava

Supervisor: Ing. Juraj Papčo, Ph.D.
Department of Theoretical Geodesy and Geoinformatics
Faculty of Civil Engineering, STU in Bratislava
Radlinského 11, 810 05 Bratislava, Slovakia

Consultant: Dr. Ir. Hans van der Marel
Department of Geoscience and Remote Sensing
Delft University of Technology
2628 CN Delft, The Netherlands

Opponents: Hon.-Prof. Dr. rer. nat. Michael Eineder
[1]Department of Aerospace and Geodesy
Technical University of Munich
Willy-Messerschmitt-Str. 1, 82024 Taufkirchen/Ottobrunn, Germany
[2]German Aerospace Center (DLR)
Remote Sensing Technology Institute, SAR Signal Processing
Oberpfaffenhofen, 82234 Weßling, Germany

Assoc. prof. Dr. Yuxiao Qin
School of Electronics and Information
Northwestern Polytechnical University
Xi'an, Shaanxi, China

Ing. Branislav Droščák, Ph.D.
Department of Geodetic Controls
Geodetic and Cartographic Institute in Bratislava
Chlumeckého 1941/4, 820 12 Bratislava, Slovakia

The executive summary was sent on: ....

The dissertation defence takes place on: ....
at the Department of Theoretical Geodesy and Geoinformatics, Faculty of Civil Engineering, Slovak University of Technology in Bratislava, Radlinského 11, 810 05 Bratislava.

....

prof. Ing. Stanislav Unčík, PhD.
The dean of the Faculty of Civil Engineering
Slovak University of Technology in Bratislava
Radlinského 11, 810 05 Bratislava

InSAR Measurements in a Geodetic Reference Frame

Abstract

Synthetic Aperture Radar Interferometry (InSAR) is a mature geodetic remote sensing technique for measuring the deformation time series of the Earth's surface with sub-centimetre accuracy in a network of natural radar scatterers. Geodetic utilization of InSAR may be limited because: (i) the displacement time series are observed at opportunistic points with low geolocation accuracy, (ii) in a datum of an arbitrary reference point with assumed zero-displacement, (iii) in difficult-to-interpret satellite's line-of-sight geometry, and (iv) with accuracy limited by the systematic effects. In this thesis, we summarize in-depth theoretical and practical particulars of using artificial radar reflectors, i.e., corner reflectors and radar transponders, to attain a reliable reference frame and quality control of datum-free InSAR measurements. We introduce a new temporal method for estimating the Signal-to-Clutter Ratio (SCR) of radar reflectors. Empirical results on a corner reflector network in the Netherlands show that the temporal method, compared to the standard method, yields a less biased and more precise estimate of the SCR, providing prediction of the InSAR phase variance, as well as the positioning precision, which are closer to the truth. We develop a dedicated InSAR time series software, GECORIS, based on the geodetic estimation theory and integrating artificial radar reflectors. We demonstrate its functionality on the corner reflector network for landslide monitoring in Slovakia. To test the reliability of radar transponders as a compact alternative to corner reflectors, we perform first multi-year experiments, achieving 0.5–1 mm phase standard deviation. However, transponders suffer from notable drawbacks: the significant radar-cross-section variations, internal electronic delays, and phase instability due to the temperature variations. Therefore, individual calibration is necessary for their precise InSAR applications. Finally, we design and test the permanent station co-locating InSAR and global navigation satellite systems (GNSS) measurements.

InSAR Merania v Geodetickom Referenčnom Rámci

Abstrakt

Družicová radarová interferometria (InSAR) je pokročilá geodetická technológia diaľkového prieskumu na určovanie časových radov deformácií zemského povrchu v sieti prirodzených radarových odrážačov so sub-centimetrovou presnosťou. Geodetické využitie InSAR je obmedzené tým, že (i) deformačné časové rady sú pozorované v a priori neznámych bodoch s nízkou presnosťou geolokácie, (ii) relatívne k ľubovoľnému referenčnému bodu s predpokladanou stabilitou, (iii) v ťažko interpretovateľnej geometrii snímania družice a (iv) s opakovateľnosťou obmedzenou systematickými chybami. V práci sumarizujeme teoretické a praktické aspekty využitia umelých radarových odrážačov, t.j. kútových odrážačov a radarových transpondérov, s cieľom zabezpečiť definovanie spoľahlivého referenčného rámca a validáciu kvality InSAR meraní. Predstavujeme novú metódu na odhad pomeru signálu k radarovému pozadiu (z angl. Signal-to-clutter ratio, SCR) radarového odrážača. Na experimentoch s odrážačmi v Holandsku ukazujeme, že táto metóda, v porovnaní s štandardnou metódou, poskytuje menej vychýlený a presnejší odhad SCR, čo zabezpečuje spoľahlivejšiu predikciu rozptylu InSAR fázových meraní, ako aj presnosti určovania polohy. Vyvíjame špecializovaný open-source softvér, GECORIS, na analýzu InSAR časových radov, postavený na teórii spracovania geodetických meraní a s integráciou umelých radarových odrážačov. Jeho využitie demonštrujeme na meraniach zo siete kútových odrážačov na monitorovanie zosuvných oblastí Slovenska. Aby sme overili spoľahlivosť radarových transpondérov ako kompaktnej alternatívy kútových odrážačov, ukutočňujeme prvé viacročné experimenty, pri ktorých dosahujeme štandardnú odchýlku 0.5–1 mm fázových meraní. Nachádzame však aj nedostatky: významné variácie intenzity radarovej odozvy, interné elektronické oneskorenia, a fázovú nestabilitu v dôsledku teplotných variácií. Preto je nevyhnutná individuálna kalibrácia pre využitie transpondérov na presné InSAR aplikácie. Na záver práce vytvárame a testujeme nový dizajn permanentnej stanice na kolokáciu meraní InSAR a globálnych družicových systémov na určovanie polohy (GNSS).

Contents

1 Introduction

Synthetic Aperture Radar (SAR) Interferometry (InSAR) is nowadays a well-established geodetic remote sensing technique gaining its place among the state-of-the-art deformation monitoring methods like levelling, tachymetry, laser scanning or Global navigation satellite systems (GNSS). InSAR time series techniques utilize regular image acquisitions from satellite-borne SAR sensors over a particular place on the Earth's surface to identify natural radar reflectors forming an 'opportunistic' geodetic network. Through InSAR processing, the temporal evolution of relative displacement over this network can be retrieved, thus allowing to monitor the impact of deformation phenomena over large areas (seismic or tectonic activity), cities and municipalities (landslides or land subsidence), or even individual structures (stability failures). Pioneering works in the field of InSAR time series by Ferretti et al. (2001) and Hanssen (2001), extended with the principles of geodetic estimation theory and stringent quality control (Kampes 2006, Guarnieri & Tebaldini 2008, Ketelaar 2009, van Leijen 2014, Samiei-Esfahany et al. 2016, Ansari et al. 2018), define the state-of-the-art, which we hereafter refer to as the *InSAR geodesy*. Millimetre-level accuracy of InSAR geodesy, comparable to the conventional geodetic monitoring techniques, was proven by several independent validation initiatives worldwide, most notably: (Ferretti et al. 2007, Hanssen et al. 2008, Marinkovic et al. 2008, Crosetto et al. 2009, Adam et al. 2009, Sadeghi et al. 2021).

1.1 Problem Statement

The precision and reliability of InSAR estimates are rarely addressed. However, the declared millimetre-level accuracy of InSAR can be only attained under the coherent conditions and the successful mitigation of systematic errors, e.g., due to the differential atmospheric delays. Different InSAR time series approaches often provide different results using the same data. It results in devaluation and misinterpretation of the reliability of the InSAR products for the wider geoscientific community. The most serious causes of mistrust in InSAR measurements are: (i) networks of natural radar scatterers are 'opportunistic', i.e., zero-order design of the geodetic network is missing; (ii) parameter estimates of the network are 'datum-free' or in a vaguely specified datum of an arbitrary reference point; (iii) the parameter estimates are usually not accompanied by the appropriate quality indicators and are increasingly affected by the systematic effects with the increasing network sizes; (iv) the displacement estimates are in a difficult-to-interpret line-of-sight geometry of the satellite; (v) the accurate displacement estimates are at 'points' of low geolocation accuracy, often missing a link to the physical objects.

Although the opportunistic character of InSAR as a remote sensing technique does not require any planning and in-advance installation of markers/benchmarks in the field, the deployment of artificial reflectors may solve some of the mentioned limitations.

Artificial radar reflectors, that is, corner reflectors or transponders, approximating ideal radar point scatterers (PS) with precisely known positions of their effective phase centres, are commonly used for SAR sensor calibration and validation, both radiometric and geometric. For InSAR applications, they may be deployed to obtain reliable measurement points with displacement time series over areas with few natural coherent scatterers. InSAR is inherently a relative technique, i.e., the phase double-differences are the first interpretable observations, and thus the estimated displacements between the radar scatterers can be regarded as a datum-free network (Hanssen 2001). A datum-free network of natural radar scatterers could be tied to a well-defined geodetic terrestrial reference frame (TRF) by co-locating SAR measurements with other geodetic observations. However, co-location of InSAR and other geodetic techniques is not trivial, as they operate in different datums, in different geometries, with different benchmarks, and at different observation times. This co-location problem could be overcome using artificial reflectors, with known local ties to the measurements of the Global Navigation Satellite System (GNSS).

The absolute positioning of radar scatterers relates to a dimensionless 2D radar datum (azimuth and range). Utilizing the range-Doppler equations, precise orbital state vectors, and an external elevation model, these positions can be transformed to a TRF (Bamler & Hartl 1998, Cumming & Wong 2005). However, geocoding errors in the order of several decimeters to meters are typically present, even if all relevant systematic geophysical and signal propagation corrections have been applied (Dheenathayalan et al. 2016, Gisinger et al. 2021). Artificial reflectors can be utilized to quantify these positioning errors. Consequently, they could improve the geolocation accuracy of a surrounding network of natural radar scatterers (Gisinger et al. 2016, Yang et al. 2019).

The methodology for analyzing the SAR time series of artificial radar reflectors has not been concisely summarized, nor are the particulars of InSAR corner reflectors and their co-location with geodetic infrastructure addressed. Moreover, the viability of long term geodetic collocation of InSAR corner reflectors is yet to be proven, especially for compact radar transponders, only recently appearing on the commercial market. For best co-location results, avoiding assumptions, a mechanical connection of corner reflector and GNSS antenna might be necessary. However, the InSAR datum connection and geodetic integration using direct co-location in observation space have been seldom studied (Mahapatra et al. 2017).

1.2 Research Objectives

Concerning the problem statement, the research objective of this dissertation is to attain InSAR measurements in a geodetic reference frame, for which the sub-objectives are:

I Contribute to the detailed documentation of InSAR estimates in terms of precision and repeatability, focusing on the geodetic community. To achieve this objective, develop an in-house and open-source InSAR time series processing framework, implementing state-of-the-art InSAR time series analysis based on the geodetic estimation theory. Focus on the quality control, limitations, and mitigation of systematic errors, such as differential atmospheric phase delays.

II Summarize the particulars of artificial radar reflectors and implement the methodology to analyze their SAR time series. Focus on the design, installation, radiometric, positioning and interferometric measurements.

III Test usability and demonstrate practical advantages of corner reflectors and radar transponders for InSAR geodesy in field conditions.

IV Design and validate a co-location station connecting inherently relative InSAR measurements to the absolute geodetic reference frame in Slovakia.

1.3 Outline

The thesis is a cumulative dissertation summarizing the contents of four peer-reviewed journal papers. The thesis contains the in-depth introduction into the InSAR geodesy and InSAR time series analysis based on the geodetic estimation theory. It includes the examples on the case study of landslide and land subsidence monitoring in Slovakia, published in the *Geosciences* journal (Czikhardt et al. 2017). The scope of this executive summary is limited to the main research contributions of the thesis. Section 2.1 contains the measurement theory and new method for estimating Signal-to-Clutter Ratio (SCR) of the radar point scatterers, such as corner reflectors. It was published in the *IEEE Geoscience and Remote Sensing Letters* journal (Czikhardt, van der Marel, van Leijen & Hanssen 2021). Section 2.2 presents new software for analyzing SAR time series of corner reflectors, with the case study of corner reflector network for landslide monitoring in Slovakia. It was published in the *Remote Sensing* journal (Czikhardt, van der Marel & Papco 2021). Section 3 reports the results of the first multi-year field tests of compact radar transponders for InSAR geodesy. It was submitted to the *IEEE Transactions on Geoscience and Remote Sensing*. Finally, Section 4 presents the new design of InSAR and GNSS co-location station. Research contributions of the thesis are summarized in Section 5.

2 Corner Reflectors for InSAR Geodesy

Corner reflectors are commonly used for radiometric and geometric SAR sensor calibration and validation, (Freeman 1992, Doerry 2008, Balss et al. 2018, Gisinger et al. 2021), SAR interferometry (InSAR) quality assessment (Ferretti et al. 2007, Quin & Loreaux 2013), InSAR applications over areas with few natural coherent reflectors (Fu et al. 2010, Garthwaite 2017), and for InSAR datum connection and geodetic integration (Mahapatra et al. 2017).

2.1 Estimating Signal-to-Clutter Ratio of InSAR Corner Reflectors From SAR Time Series

SAR calibration, positioning, and InSAR applications require a precise and unbiased estimation of the Signal-to-Clutter Ratio (SCR): the ratio of the Radar-Cross-Section (RCS) of the reflector and the power of its background clutter. The SCR estimate is used to estimate the InSAR phase variance (Dheenathayalan et al. 2017) and the absolute positioning accuracy (Bamler & Eineder 2005) of point targets, such as corner reflectors, for geodetic applications.

The standard method for estimating RCS and SCR of point targets involves spatial numerical integration of pixel intensity values in square-law detected SAR images (Gray et al. 1990, Freeman 1992). It assumes that the background clutter over the integrated area exhibits the same statistical properties as its surroundings, i.e. spatial ergodicity. However, for geodetic applications using medium-resolution SAR data clutter in the surrounding pixels is often not representative and sometimes contains other point scatterers, violating the assumption of spatial ergodicity.

Here we propose to estimate the SCR of small-to-medium-sized corner reflectors using SAR time series. The objective is to obtain an unbiased and precise average SCR estimate under the assumption on the temporal ergodicity. SAR time series are currently in abundance thanks to the operational SAR satellite missions, such as Sentinel-1. A secondary objective of the proposed method is to utilize the time series of RCS to track the reflector performance, and identify possible outliers due to damage, debris accumulation or other external factors.

2.1.1 Methodology

A point scatterer response in the SAR image is a 'sinc-like' 2D impulse response function (IRF) in azimuth and range (Bamler & Hartl 1998). A corner reflector is an approximation of an ideal radar point scatterer, P. Considering single-look-complex (SLC) SAR images in the zero-Doppler geometry, the phasor measurement y_P per resolution cell R_P containing a dominant point scatterer P consists of a real $\mathrm{Re}\{y_P\}$ and an imaginary $\mathrm{Im}\{y_P\}$ signal component:

$$y_P = \mathrm{Re}\{y_P\} + j\mathrm{Im}\{y_P\} = \sum_{i \in R_P} A_i \exp(j\psi_i), \tag{1}$$

which is the coherent summation of the backscatter from the point scatterer P and the scattering contributions of its surroundings—the clutter—within the same resolution cell R_P, where A is the amplitude and ψ the phase.

Radar Cross Section The power (intensity) of the signal in (1) is $A_P^2 = \mathrm{Re}\{y_P\}^2 + \mathrm{Im}\{y_P\}^2$. The pixel intensity is stored in the SLC image as a *digital number* (DN). Scaling factors are used to express DN in terms of a specific backscattering coefficient.

In the context of *point scatterers* (PS), DN is converted to RCS, which describes the ability of a point scatterer to intercept incident energy with an effective cross-sectional area and reflect it in the direction of a radar receiver (Doerry 2008). For an idealized PS response in the absence of clutter, the RCS is the integral of the power (signal energy) under its IRF (Gray et al. 1990).

RCS is strictly related to PS. For *distributed scatterers* (DS), a dimensionless *backscattering coefficient*, σ_0, is generally used to describe their mean reflectivity per unit area of a horizontal surface. Contrary to σ_0, *radar brightness*, β_0, is independent of the radar signal's local incidence angle, as its area normalization is in the slant-range direction (Raney et al. 1994). Radar brightness is computed via (Miranda & Meadows 2015):

$$\beta_0 = \left(\mathrm{DN}^2 - \eta\right) \alpha_{\mathrm{DN}}^{-2} K^{-1} \tag{2}$$

where the calibration constant K and the pixel scaling factor α_{DN} are annotated in the metadata of SLC products. α_{DN} is given as a pixel look-up table (LUT). The thermal noise correction η, i.e. the Noise-Equivalent-Sigma-Zero (NESZ), is applied if available in the LUT annotation (e.g. in the case of Sentinel-1 data (Piantanida et al. 2017)). Given the local incidence angle, θ, σ_0 is readily obtained from β_0 as $\sigma_0 = \beta_0 \sin\theta$. Henceforth, we assume a dimensionless, calibrated, and noise-corrected amplitude measurement, A, obtained from (2) as $A = \sqrt{\beta_0}$.

Amplitude Probability Density and SCR Distributed scatterers (DS) can be considered as the coherent summation of many random elementary scatterers within a resolution cell. Therefore, the central limit theorem applies, and the probability density function (PDF) of a DS complex phasor per image pixel is circular Gaussian (Dainty 1975, Bamler & Hartl 1998). Consequently, its amplitude A (1) is Rayleigh distributed with (Hanssen 2001)

$$\mathrm{PDF}(A|\sigma) = \frac{A}{\sigma^2} \exp\left[-\frac{A^2}{2\sigma^2}\right] \tag{3}$$

where σ is a scale parameter, related to the expected value of the power by $\mathbb{E}(A^2) = 2\sigma^2$, and the phase $\psi \in [-\pi, \pi)$ is uniformly distributed (Oliver & Quegan 2004).

Point scatterers (PS), on the other hand, can be considered a signal determined by their physical properties and coherence. However, they are typically superimposed on the surrounding scatterers within the same resolution cell, i.e. the clutter. The ratio between the signal and the clutter is described by the SCR, and is a metric for the noise in the PS. Consider a PS characterized by complex phasor y. Clutter in the same resolution cell introduces circular Gaussian noise n characterized by its expected value $\mathbb{E}(n) = 0$ and variance σ_n^2 for both its real and imaginary components. The PS amplitude A (1) follows a Rice distribution (Ferretti et al. 2001, Oliver & Quegan 2004):

$$\mathrm{PDF}(A|\mu, \sigma_n) = \frac{A}{\sigma_n^2} I_0\left(\frac{A\mu}{\sigma_n^2}\right) \exp\left[\frac{-\left(A^2 + \mu^2\right)}{2\sigma_n^2}\right] \tag{4}$$

where I_0 is the modified-Bessel function of the first kind with order zero and $\mu = \mathbb{E}(A)$ is the expected value of the amplitude. The shape of the Rice distribution is determined by the SCR:

$$\mathrm{SCR} = \frac{\mu^2}{2\sigma_n^2} \tag{5}$$

which is the ratio of a reflector's signal power to the power of the surrounding clutter within the resolution cell. Note that for clutter only, the Rice PDF transforms to a Rayleigh PDF driven solely by variance $\sigma_n^2 = \mathbb{E}(A^2)/2$.

Spatial SCR estimation method If SAR sensor and processing gain factors are known, and DN values, see (2), are scaled to pixel intensities, the standard RCS estimation formula (Gray et al. 1990, Freeman 1992) can be rewritten as (Miranda & Meadows 2015, Schmidt et al. 2020):

$$\mathrm{RCS} = \frac{I_P}{K}\frac{P_A}{C_F} \tag{6}$$

where I_P is the total (integrated) power in the mainlobe (which is not directly observable due to the superimposition with clutter occupying the same resolution cell as the point target), C_F is the relative power in the sidelobes and P_A is the sample (pixel) area. As the IRF is finitely sampled by the SAR image pixels, oversampling and numerical integration is employed within the estimation process. The components of (6) are approximated as follows:

I_P We estimate the background clutter C from four areas (quadrants) outside the cross-shaped area of the IRF, assuming spatial ergodicity. We subtract C from all pixel intensities within a center area of 2 by 2 resolution cells (half-power width of IRF), centered at the point target. We integrate corrected pixel intensities within the center area, which yields I_P.

C_F We estimate the sidelobe energy from pixels spanning the IRF cross-hair within 10 by 10 resolution cells. We then compute the ratio between the total energy in the sidelobes (excluding the mainlobe) and the energy in the mainlobe, i.e., the integrated sidelobe ratio ISLR. The relative power in the sidelobes is $C_F = 1/(1 + \mathrm{ISLR})$.

K calibration constant as annotated in the SLC metadata.

P_A azimuth times slant-range pixel spacing in meters.

The SCR is obtained as the ratio of the estimated I_P and the estimated clutter power C, multiplied by the mainlobe area $\Delta_{\mathrm{mainlobe}}$:

$$\mathrm{SCR} = \frac{I_P}{C \cdot \Delta_{\mathrm{mainlobe}}}. \tag{7}$$

Temporal SCR estimation method An alternative to the spatial SCR estimation method is to compute the average SCR from time series of the instantaneous 'apparent RCS', using the *peak* method (Gray et al. 1990, Ulander 1991), and maximum likelihood estimation (MLE) to estimate the mean RCS and the clutter. Defining the resolution as the half-power width (−3 dB) of the IRF mainlobe, multiplying the IRF peak intensity with the resolution cell area yields the volume of a rectangular box which is the same as the volume (power) under a 2D IRF.

The original peak method assumes that the space-averaged clutter and mean system noise are used to correct the peak response. However, the clutter power estimated from nearby pixels in medium-resolution SAR imagery in areas with spatially varying clutter may be inaccurate. Therefore, we intentionally omit this correction in the 'apparent RCS' computation:

$$\mathrm{RCS} \approx \beta_0 \cdot \Delta_{az}\Delta_r \quad [\mathrm{m}^2] \tag{8}$$

where $\Delta_{\mathrm{az/r}}$ are the azimuth and range resolution respectively. Peak and clutter contributions are separated from the amplitude time series assuming temporal ergodicity. Given a reasonably large time series (>20 images), two independent clutter power estimates are obtained by:

1. a maximum likelihood fit of a Rayleigh distribution, see (3), to the amplitude time series of the site prior to the installation of the reflector, to estimate the power of the clutter, and

2. a maximum likelihood fit of a Rice distribution to the peak amplitude time series of the reflector after installation, to separate the clutter and point scatterer contributions via its two parameters, see (4). The first parameter, $\hat{\mu}_{\text{MLE}}$, multiplied by the resolution cell area yields the reflector's RCS, see (8). The second parameter, $\hat{\sigma}_{\text{MLE}}$, represents the power of the clutter while the reflector is in place (provided its statistical properties are not undergoing significant temporal changes). The ratio of the two parameters is the estimate of the SCR, see (5):

$$\widehat{\text{SCR}} = \frac{\hat{\mu}^2_{\text{MLE}}}{2\hat{\sigma}^2_{\text{MLE}}}. \tag{9}$$

Note that the sample mean and the standard deviation are biased estimators for μ and σ, although their ratio, known as the normalized amplitude dispersion, is generally used as the phase standard deviation proxy in InSAR applications (Ferretti et al. 2001). If the assumption on the stationarity of the clutter is violated, it still yields the unbiased average SCR estimate, although not fully representative for the instantaneous RCS (considering, e.g., seasonal or secular variations). Absolute radiometric calibration, however, is not the primary objective of the temporal estimation method. Potential outliers in the 'apparent' RCS (e.g. due to debris accumulation) are readily handled in time series analysis using a threshold of three median absolute deviations (MAD), thus ensuring the reflector's RCS does not significantly vary in time.

2.1.2 Experiments

The viability of the proposed method is tested on Sentinel-1 C-band SLC time series in two different experiments in the Netherlands. The first experiment uses a corner reflector network with 24 sites (48 reflectors), see Fig. 1.

(a) (b) (c)

Figure 1: (a) Network of 24 Integrated Geodetic Reference Stations (IGRS), (b) CRDS reference reflector used in the second experiment, (c) IGRS DBFT reflector used in both experiments.

The second experiment uses two proximate corner reflectors. For each experiment, a time series of three years with a 6-day acquisition interval is collected, from April 2017 until April 2020, including one year of measurements before installation. For each reflector, an image patch of 10×10 resolution cells is selected and oversampled by a factor 32 in the frequency domain using zero-padding. Then, we estimate the precise peak position and amplitude by fitting a 2D elliptic paraboloid over a small image sub-patch, centered at the oversampled amplitude maximum of the initial image patch (Balss et al. 2018).

Corner reflector network experiment Both the spatial and the temporal RCS and SCR estimation methods were applied on ascending track 88 and descending track 139 covering the network of

Integrated Geodetic Reference Stations (IGRS) in Groningen, see Fig. 1a. Each of the 24 IGRS stations consists of a GNSS antenna and two back-flipped triangular trihedral corner reflectors, see Fig. 1c, with an inner edge length of 0.9 m and a corresponding theoretical RCS of 29.5 dBm^2 at boresight for C-band (Hanssen 2017). Figs. 2a and b show the distribution of the observed radar brightness values for a particular resolution cell, before and after corner reflector installation, respectively. The corresponding distribution functions match with the Rayleigh and the Rice distribution. This sustains our assumption on the validity of these functions, see section 2.1.1.

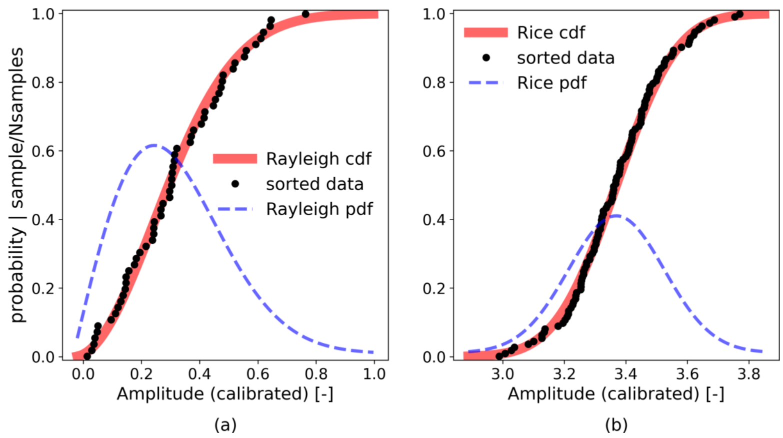

Figure 2: Sorted and scaled amplitude data of a resolution cell before (a) and after (b) corner reflector installation, corresponding to the background clutter and the point target response, respectively. The background clutter follows a Rayleigh distribution whereas the reflector follows a Rice distribution.

Fig. 3 shows scatter plots of the temporally averaged results for all 48 reflectors.

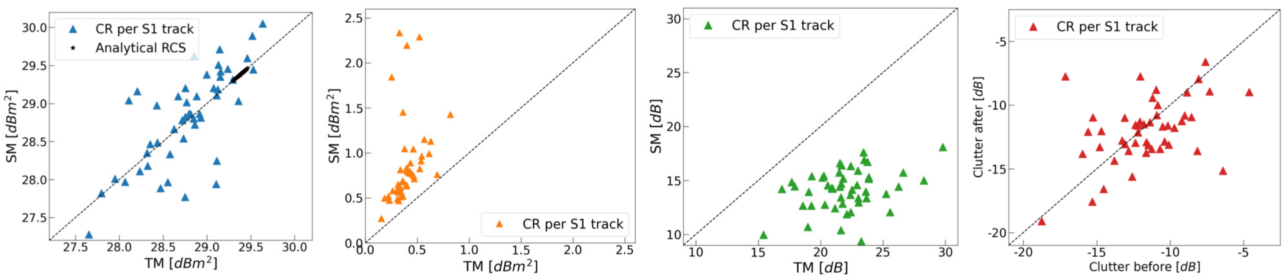

(a) Average RCS (b) RCS standard deviation (c) Average SCR (d) Clutter power

Figure 3: (a) - (c) Comparison of the spatial method (SM) and the temporal method (TM) for RCS and SCR estimation of 48 corner reflectors (CR) on three years of Sentinel-1 time series from ascending track 88 and descending track 139. (d) Clutter power estimated by the TM before/after corner reflector deployment. Each triangle represents a single CR of the network.

Fig.3a confirms that the estimated RCS values of the reflectors by the temporal method (TM) are comparable to the spatial method (SM). The mean and standard deviation of the differences is 0.04 dB and 0.42 dB respectively. The black dots show the analytical RCS values computed using a geometric optics simulation (Doerry 2008, Groot 1992), taking into account the corner reflector alignment for each acquisition. Fig. 3b shows that the precision of the RCS estimates, expressed as the standard deviation of the time series, is significantly better for the temporal method. This is mainly because the temporal method does not use the instantaneous clutter estimates to correct (8), whereas the spatial method does. The higher precision of the temporal method is also justified considering the reported 0.25 dB radiometric stability (1 sigma) of Sentinel-1 SLC data (CLS 2020). Fig. 3c shows that the differences between the spatial and temporal methods for SCR estimation are significant. This is caused by the different strategies of clutter estimation. While the spatial method uses samples outside the IRF (which represents surfaces tens to hundreds of meters away from the actual reflector position in case of medium-resolution data), the temporal method uses samples directly from the reflector, albeit assuming temporal ergodicity of the SCR in the time series. Finally, Fig. 3d depicts an independent validation of clutter power estimates using the temporal method, see section 2.1.1. The clutter power values estimated from time series after reflector installation (Rice distribution fit, scale parameter) differ by 0.05 dB in the mean with 3.84 dB standard deviation from the independently estimated values from the time series before reflector's deployment (Rayleigh distribution fit).

The estimated SCR can be used to predict the peak position variance in the radar coordinates (azimuth and range) (Bamler & Eineder 2005). We do the reverse, and use the observed peak position variance to compare with the predictions computed by the spatial and the temporal method. The observed sub-pixel peak positions were corrected for the effects of reference frame motion, solid earth tides, atmospheric signal delay and Sentinel-1 specific processor biases in both azimuth and range, as reported by (Small & Schubert 2019, Gisinger et al. 2021). Fig. 4 shows that the positioning standard deviations predicted by the spatial method are higher than the observed standard deviations. On the other hand, standard deviations predicted by the temporal method are equal or slightly lower. The latter is what we expect: the predicted values are the Cramer-Rao Lower Bounds (CRLB) and should be smaller than those observed, and the observed standard deviation is affected by other errors, such as variations in tropospheric signal delay, which could not be completely mitigated.

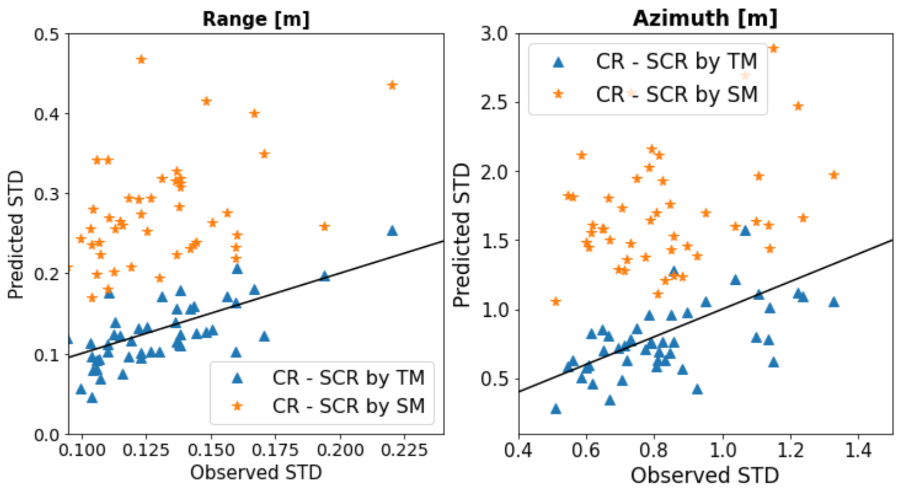

Figure 4: Predicted versus estimated standard deviations (STD) of observed peak positions in azimuth and range (in meters) of 150 Sentinel-1 time series. Each point represents a single corner reflector.

Short baseline experiment An experiment to evaluate the bias in the estimated SCR is performed on a test site where two corner reflectors, 'CRDS' and 'DBFT', form a very short baseline of 102 m length. Under such circumstances, the clutter can be considered the main component of the phase variance. CRDS is square-based trihedral, see Fig. 1b, with an inner edge length of 1.425 m and a corresponding peak-RCS of 40.7 dBm^2 for C-band, while DBFT is a back-flipped triangular trihedral with an inner edge length of 0.9 m and a corresponding peak-RCS of 29.5 dBm^2 for C-band.

The CRLB, $\sigma_{\psi}^{\mathrm{SCR}}$, (Dheenathayalan et al. 2017) of the single-epoch phase measurement ψ, computed from the estimated SCR and propagated to the double-differenced InSAR phases, $\sigma_{\Delta\phi}^{\mathrm{SCR}}$, with $\sigma^2_{\Delta\phi_{i,j}} = 2\sigma^2_{\psi_i} + 2\sigma^2_{\psi_j}$, is compared to the standard deviation $\hat{\sigma}_{\Delta\phi}$ estimated on the actual observed double-differenced phase measurements. Results for different SCR estimation methods are shown in Table 1. For the spatial method we used the temporally averaged SCR. The empirical standard deviation, $\hat{\sigma}_{\Delta\phi}$, is computed from the detrended double-differenced phase measurements of two descending Sentinel-1 tracks spanning 2.5 years, i.e., 150 acquisitions, see Fig **??**. Considering the sensor noise,

Table 1: SCR-derived versus observed double-differenced phase standard deviations, in millimeters

		$\sigma_{\psi}^{\mathrm{SCR}}$		$\sigma_{\Delta\phi}^{\mathrm{SCR}}$		
Track	Reflector	SM	TM	SM	TM	$\hat{\sigma}_{\Delta\phi}$
DSC t037	CRDS	0.22	0.10	1.00	0.47	0.43
	DBFT	0.67	0.32			
DSC t110	CRDS	0.21	0.11	1.13	0.47	0.44
	DBFT	0.77	0.31			

not accounted for by the CRLB prediction, the comparison shows that the temporal method provides a more realistic, unbiased phase variance prediction, hence SCR estimate, while the spatial method overestimates it, even if a sizeable temporal average is used.

2.1.3 Discussion and Conclusions

The pros and cons of the spatial and temporal SCR estimation methods for corner reflectors are summarized in Tab. 2.

Table 2: Comparison of the spatial and the temporal method for SCR estimation.

Spatial method (SM)	**Temporal method (TM)**
advantages	
• Epoch-wise description of IRF • Instantaneous RCS representative of secular or seasonal effects • Invariant to resolution values	• Higher precision • Unsupervised clutter estimation • Less biased SCR estimate in a complex environment
disadvantages	
• Assumption on spatial ergodicity of the clutter • Biased SCR estimate in case of close proximity of other point scatterers or significant clutter	• Assumption on temporal ergodicity of the clutter, time series needed • Precise resolution values needed • Sidelobes not accounted for

The significant standard deviation of the clutter power differences, estimated by the temporal method, shows that the temporal ergodicity assumption may be violated. Nonetheless, for small-sized InSAR corner reflectors with proximate point scatterers, this assumption is often more realistic than the assumption of spatial ergodicity. The assumption of spatial ergodicity cannot be fulfilled as the surroundings of the reflectors are often not homogeneous random scatterers but may contain several other point scatterers. The temporal SCR estimate, invariant to the potential RCS estimate bias, is more realistic with respect to the standard deviation of the phase measurement and positioning precision, which are imperative for InSAR applications.

2.2 GECORIS: An Open-Source Toolbox for Analyzing Time Series of Corner Reflectors in InSAR Geodesy

Organizations operating or deploying networks of corner reflectors (CR)—such as the Australian Corner Reflector Array (Garthwaite et al. 2015b), the network of Integrated Geodetic Reference Stations (IGRS) (Hanssen 2017, Kamphuis 2019) in the Netherlands, or the Slovakian Corner Reflector

Networks for landslide monitoring—require a dedicated tool for their monitoring. This tool shall facilitate the operational analysis of SAR time series of reflectors to track their measurement quality: (i) with respect to the design requirements; (ii) over time; (iii) to identify potential problems, such as damage or debris accumulation; and (iv) estimate their displacement time series. To the authors' knowledge, such a tool is not currently available as free and open-source software (FOSS) for the geodetic and SAR community.

Therefore, the objectives of this work are (i) to present a standard procedure to analyze SAR time series of artificial radar reflectors to estimate their Radar Cross Section, Signal-to-Clutter Ratio and InSAR displacement time series, (ii) to implement this procedure into an efficient, open-source toolbox, (ii) to validate the performance of the developed toolbox on the networks of corner reflectors in Slovakia.

2.2.1 Implementation

In this section, we describe GECORIS—A FOSS Geodetic Corner Reflector (In)SAR toolbox developed in Python. Its main objective is to facilitate the analysis of the SAR time series of artificial radar reflectors, either corner reflectors or transponders. Standard data I/O modules are adopted from the FOSS Sentinel's Application Platform (SNAP) (ESA 2021). The flowchart of the toolbox is given in Fig. 6.

The fully automated process of the toolbox is initially driven by the station log file containing information on the reflector type, its geometry and orientation, coordinates of its phase centre for ascending/descending orbits, and installation date. For each SAR data stack, the time series analysis consists of the following steps:

1. **Positioning of reflectors:** The primary SAR observables: azimuth time t and range time τ correspond to zero-Doppler geometry, which is at the instant of closest approach of a satellite with respect to the scatterer P—i.e., velocity vector of the sensor is perpendicular to the line-of-sight (LOS) between the sensor and the scatterer. Consequently, the Doppler shift at this instant is zero. The related range-Doppler observation equations are (Cumming & Wong 2005):

$$
\begin{aligned}
\|\boldsymbol{S}(t)-\boldsymbol{P}\|\frac{2}{c}-\tau &= 0 \\
\frac{\dot{\boldsymbol{S}}(t)\cdot(\boldsymbol{S}(t)-\boldsymbol{P})}{\left\|\dot{\boldsymbol{S}}(t)\right\|\cdot\|(\boldsymbol{S}(t)-\boldsymbol{P})\|} &= 0
\end{aligned}
\tag{10}
$$

   where $\boldsymbol{P}$ is the position vector of a scatterer in the Terrestrial Reference Frame (TRF), $\boldsymbol{S}$ and $\dot{\boldsymbol{S}}$ are the position and velocity vectors of the satellite (the antenna phase centre) at the zero-Doppler azimuth time t. A reflector position in the radar datum of each SLC is obtained by transforming the GNSS-derived TRF coordinates of its phase centre. The reverse solution of range-Doppler equations (10) is used, utilizing precise orbit state vectors (Peter et al. 2017) and metadata of each SLC.

2. **Reflector response extraction:** Image patch surrounding reflector position is first created. We perform oversampling of SLC data in the frequency domain by zero-padding. When oversampling Sentinel-1 data, special care is needed because of the linear frequency modulation introduced by the Terrain Observation with Progressive Scan (TOPS) acquisition mode. Oversampling must be performed on the deramped and demodulated SLC data, following the procedure described in Yague-Martinez et al. (2017), Miranda (2017). For each reflector's SLC image patch: (i) A local maximum is identified in a small search window of 1×1 resolution cell around the initial reflector position in the oversampled data. (ii) Elliptic paraboloid is fitted in a smaller search window (9×9 subsampled pixels) centered on the maximum to refine the peak coordinates and amplitude estimate. This procedure guarantees the peak identification precision of 1/100 pixel (Balss et al. 2018).

3. **Absolute positioning errors** (APE) are epoch-wise differences between the detected subpixel peak coordinates and the expected radar coordinates computed from the precise TRF positions via the inverse range-Doppler equations, while re-introducing all SAR timing biases. The APE in range (rg) and azimuth (az) is computed as:

$$\begin{aligned} \mathrm{APE}_{\mathrm{rg}} &= \left(\tau_{\text{peak, IPF}} - \tau_{\text{predicted}}\right) \cdot c \\ \mathrm{APE}_{\mathrm{az}} &= \left(t_{\text{peak, IPF}} - t_{\text{predicted}}\right) \cdot v_{\text{zeroDoppler}}, \end{aligned} \tag{11}$$

where $v_{\text{zeroDoppler}}$ is the satellite's ground-track zero-Doppler velocity. $\tau_{\text{peak, IPF}}$ and $t_{\text{peak, IPF}}$ are the azimuth and range time, respectively, of the sub-pixel peak positions in the SLC images as processed by the Sentinel-1's instrument processing facility (IPF). Predicted timings, $\tau_{\text{predicted}}$ and $t_{\text{predicted}}$, consist of individual timing biases:

$$\begin{aligned} \tau_{\text{predicted}} &= \tau_{\text{ITRF}} + \Delta\tau_{\text{SET}} + \Delta\tau_{\text{tropo}} + \Delta\tau_{\text{iono}} + \Delta\tau_{\text{Doppler}} \\ t_{\text{predicted}} &= t_{\text{ITRF}} + \Delta t_{\text{SET}} + \Delta t_{\text{bistatic}} + \Delta t_{\text{FM-rate}} \end{aligned} \tag{12}$$

where:

- *ITRF* are positions directly obtained solving the range-Doppler equations from GNSS-determined coordinates in ITRS (ITRF2014 reference frame) at the particular acquisition epoch. The initial coordinates in ETRS89 (ETRF2000 reference frame) are first transformed to ITRS at the particular acquisition epoch, hence reflecting the plate motion.
- *SET* are timing corrections computed from topocentric solid earth tides displacements, hence transforming from a 'tide-free' position (ITRF) to the instantaneous position as seen by the satellite (adding permanent 'mean-tide', as well as a periodic components of tidal displacement using IERS SET displacement models (IERS 2021)).
- *tropo* is the range timing correction for the slant tropospheric signal delay (modelled using ECMWF ERA5 model (Hersbach & Dee 2016)).
- *iono* is the range timing correction for the slant ionospheric signal delay (modelled using CODE IGS global ionospheric model (IGS 2021)).
- *bistatic* is the residual bistatic correction of the Sentinel-1 IPF in the azimuth timing,
- *Doppler* are Doppler-centroid-induced range timing corrections, and
- *FM* are FM-rate mismatch of Sentinel-1 IPF in the azimuth timing (Gisinger et al. 2021).

An example of timing correction magnitudes, recomputed in meters, for the trihedral corner reflector with 22 dB SCR, which is located at 49.051° latitude, 21.326° longitude and 328 m ellipsoidal height, is shown in Fig. 5.

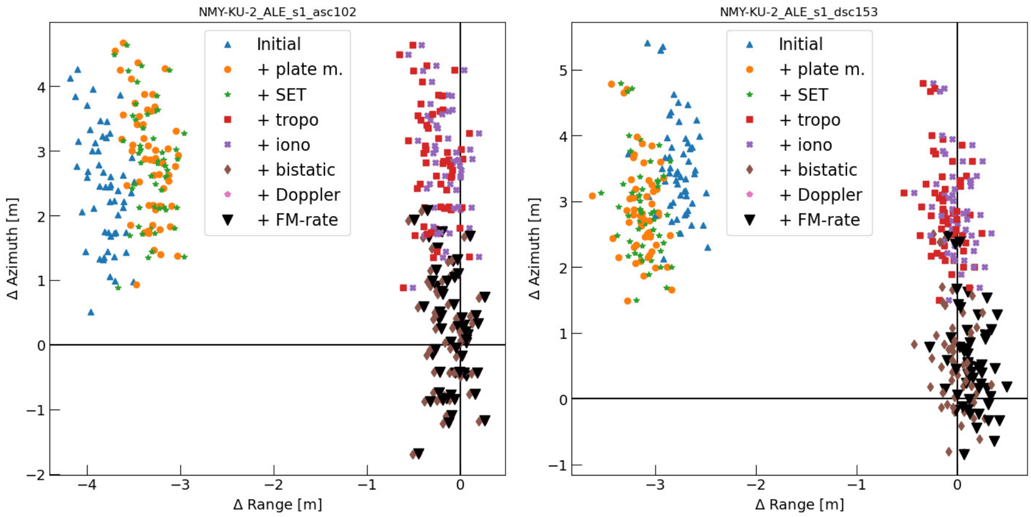

(a) ascending (b) descending

Figure 5: The influence of the individual SAR positioning corrections on the double corner reflector with 22 dB Signal-to-Clutter Ratio (SCR). Each scatter represents a single Sentinel-1 acquisition.

Considering that all systematic timing corrections have been applied, the SAR positioning accuracy limit is imposed by the scatterer's SCR (Eq. (5)). Positioning CRLB for point scatterers with SCR > 1 dB is (Bamler & Eineder 2005):

$$\sigma_{range/azimuth} \approx \frac{\sqrt{3}}{\pi\sqrt{2}} \cdot \frac{\Delta_{r/az}}{\sqrt{SCR}}. \tag{13}$$

4. **Outlier detection** using a threshold of three median absolute deviations (MAD).
5. **SCR estimation** by following methodology in Section 2.1.1.
6. **InSAR time series analysis:** The displacement time series of corner reflectors (CR) are estimated using the geodetic InSAR time series methodology, incorporating PS. For all SLC image patches, flattened and topography-corrected interferograms are generated. Then, InSAR processing is performed by the following steps:

   (i) High-quality, coherent point PS candidates are identified using a strict threshold of 0.2 on the normalized amplitude dispersion (Ferretti et al. 2001), considering only the mainlobes.

   (ii) CR and the PS candidates are connected using Delaunay triangulation to form a first-order estimation network.

   (iii) The phase corrections due to the sub-pixel position (Yang et al. 2020) are evaluated.

   (iv) Variance Component Estimation (VCE) (Teunissen & Amiri-Simkooei 2008) is performed to obtain an initial diagonal variance-covariance matrix of the phase time series. A priori phase variances of CR are predicted using the estimated SCR. The CRLB, evaluated by Dheenathayalan et al. (2017) for reflectors with SCR > 1 dB, i.e., even for small-sized reflectors, is:

$$\sigma_{d_{\mathrm{LOS}}} = \frac{\lambda}{4\pi}\sqrt{\frac{2}{2\ \mathrm{SCR} - \sqrt{3}/\pi}}, \tag{14}$$

   expressed from phase variance in terms of the standard deviation of the LOS displacement using wavelength λ.

(v) Temporal ambiguities in the double-differenced phases per arc are solved using the integer least-squares estimator (Kampes & Hanssen 2004, van Leijen 2014) and the LAMBDA method (Teunissen 1993).

(vi) Ambiguities per arcs are then integrated spatially (van Leijen 2014) using a selected reference CR or the datum-free network solution.

(vii) The Atmospheric Phase Screen (APS) is estimated from the unwrapped phases using spatio-temporal filtering, variogram fitting and kriging interpolation (van Leijen 2014).

(viii) The unwrapped phase time series, corrected for the APS, are used to estimate the residual heights and displacement model parameters of the CR and PS.

(ix) The phase residuals are then converted to the LOS displacement time series. The outliers, identified in the RCS time series, are discarded.

(x) Finally, decomposition of the cross-track LOS displacements of CR to the vertical and horizontal components is done by solving the set of linear equations (Ketelaar 2009).

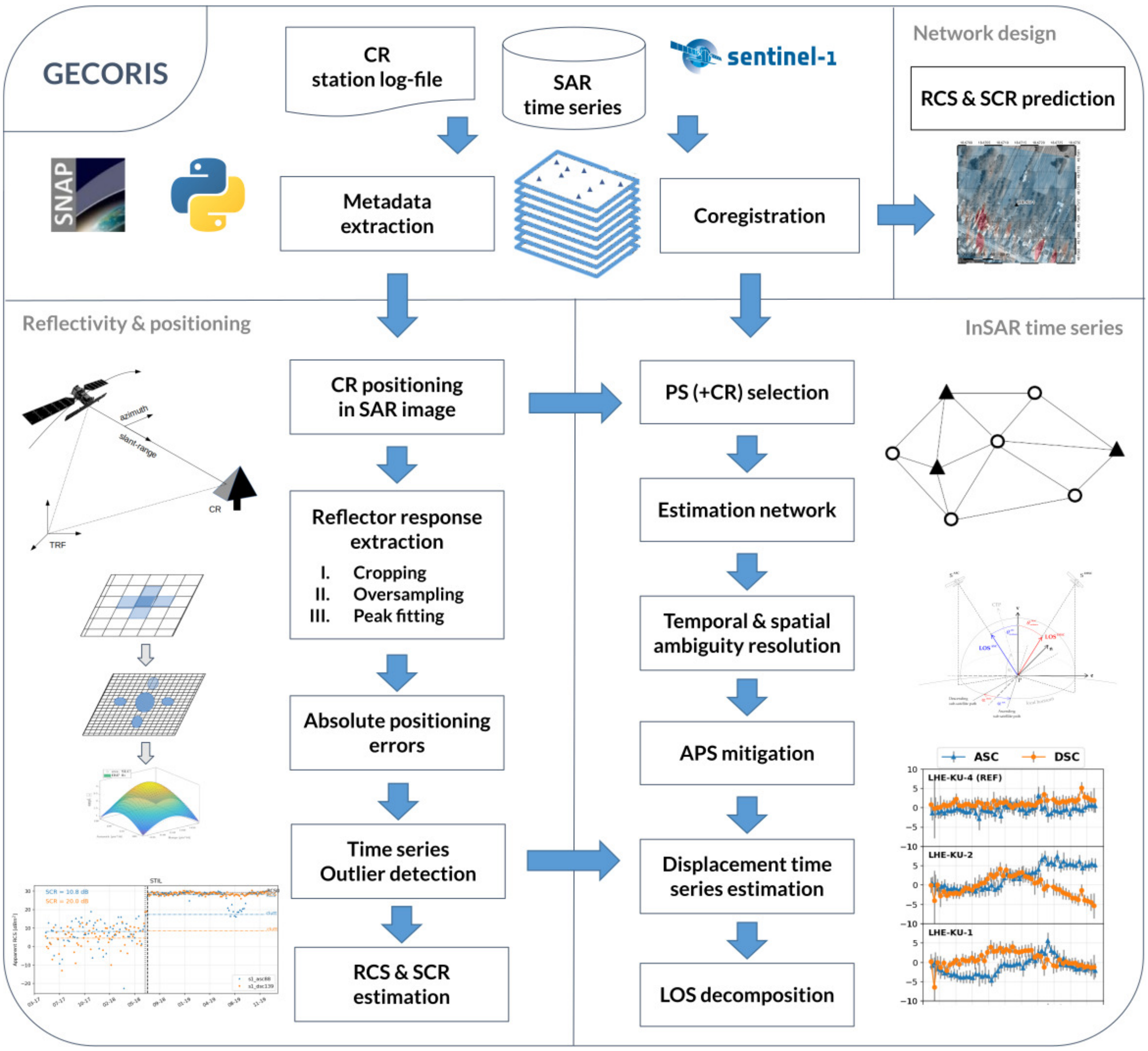

Figure 6: Flowchart of the Geodetic Corner Reflector (In)SAR (GECORIS) toolbox.

2.2.2 Case Study

Here, we use the GECORIS toolbox to analyze the Sentinel-1 measurements of a corner reflector network.

Corner Reflector Network Three networks of corner reflectors (CR) were built for landslide monitoring in Slovakia under the authority of the Slovakian State Geological Institute of Dionyz Stur (SGIDS). Seven CR are in the Upper Nitra region, and sixteen CR are in the Kosice Basin. The CR were deployed in February 2020. All CR are double back-flipped square trihedrals (DBST), that is, consisting of one reflector for ascending and one reflector for descending orbits, with inner-leg lengths of 0.76 m (Fig. 7a). Using back-flipped reflectors has an advantage of their bore-sight alignment (~35.3° zenith angle) with the average local incidence angle of the Sentinel-1 IWS acquisitions (~37.6°). DBST, being double reflectors, are oriented northwards with their central plate to minimize the unavoidable azimuth misalignment (approximately 11° for Central Europe) in ascending and descending directions. Given the geometry and orientation of the C-band Sentinel-1 measurements covering the case study areas, DBST yields an average analytical RCS of 33.5 dBm^2. The central plate of the DBST reflectors includes the mounting console for precise co-location with a geodetic GNSS antenna. Precise CR positions were measured by two, six-hour-long, static GNSS observation sessions using geodetic-grade Trimble receivers.

The limitations imposed by the radar clutter must be considered when choosing optimal locations for CR. Therefore, for planning purposes, the toolbox was used to produce maps of the expected SCR over the potential sites. One year of Sentinel-1 time series (>60 SLC) from the period before the CR were deployed are used for the clutter estimation. Using the simple thresholding approach, given the requirement on the LOS displacement standard deviation, $\sigma_{d_{LOS}}$, of <0.5 mm, the required SCR is >20 dB, see Eq. (14). Hence all areas, which meet this condition and are separated at least two resolution cells in the range and azimuth directions from nearby point scatterers, can be considered viable for the CR. Nonetheless, it is recommended to consider also in situ information.

Results Once CR are permanently installed, the toolbox is used to assess their SAR measurement performance. We analyze one year of Sentinel-1 time series for the CR performance testing and InSAR analysis. Fig. 7b shows RCS time series of the particular DBST reflector at The Upper Nitra. The dashed vertical line in the figure represents the date of the reflector deployment and proper bore-sight alignment. The horizontal lines denoted as *RCS* and *clutt* represent the estimated reflector's temporal average RCS and the clutter power, respectively. The horizontal line, denoted as *RCS0*, represents the analytical RCS. The dashed red circle marks the outliers detected during the winter months, possibly caused by the snow clogging in the reflectors.

Comparing the predicted and estimated RCS and SCR in Tab. 3 we test whether the CRs meet the monitoring requirements. Despite the varying differences of 1–3 dB between the estimated and the predicted SCR, The Upper Nitra reflectors all attain the average SCR above 20 dB. The 3 dB SCR loss at 20 dB SCR accounts to ~2.4° phase error increase (equivalent to 0.2 mm at C-band).

Fig. 7(c) shows LOS displacement time series of the reflector estimated using InSAR analysis. To verify the stability of the reference CR (LHE-4), we show the results of the datum-free solution. The error bars correspond to the two-sigma intervals given by the estimated SCR and scaled by the variance factors of individual acquisitions. The cross-track LOS displacement time series are transformed to the vertical and horizontal displacement time series, see Fig. 7(d). The time series reveal a nonlinear motions, predominantly in the west-ward direction, which is in agreement with the slope orientation of the landslide. The seasonal effect in vertical direction, that is, few millimeters of uplift following winter 2019/20, could be the consequence of the extrusion of the pillars carrying the CR, as this effect is not so apparent on the nearby PS. The displacement acceleration in September/October 2020 follows periods of significant precipitation, confirming the landslide's reaction to the underground water accumulation (Ondrejka et al. 2016, Czikhardt et al. 2017). We have interpolated the time series by the cubic splines, assuming that the model residuals are representative of the phase noise. The standard deviations of the model residuals vary between 0.6–0.9 mm for the ascending orbit and between 0.7 mm–1.3 mm for the descending orbit.

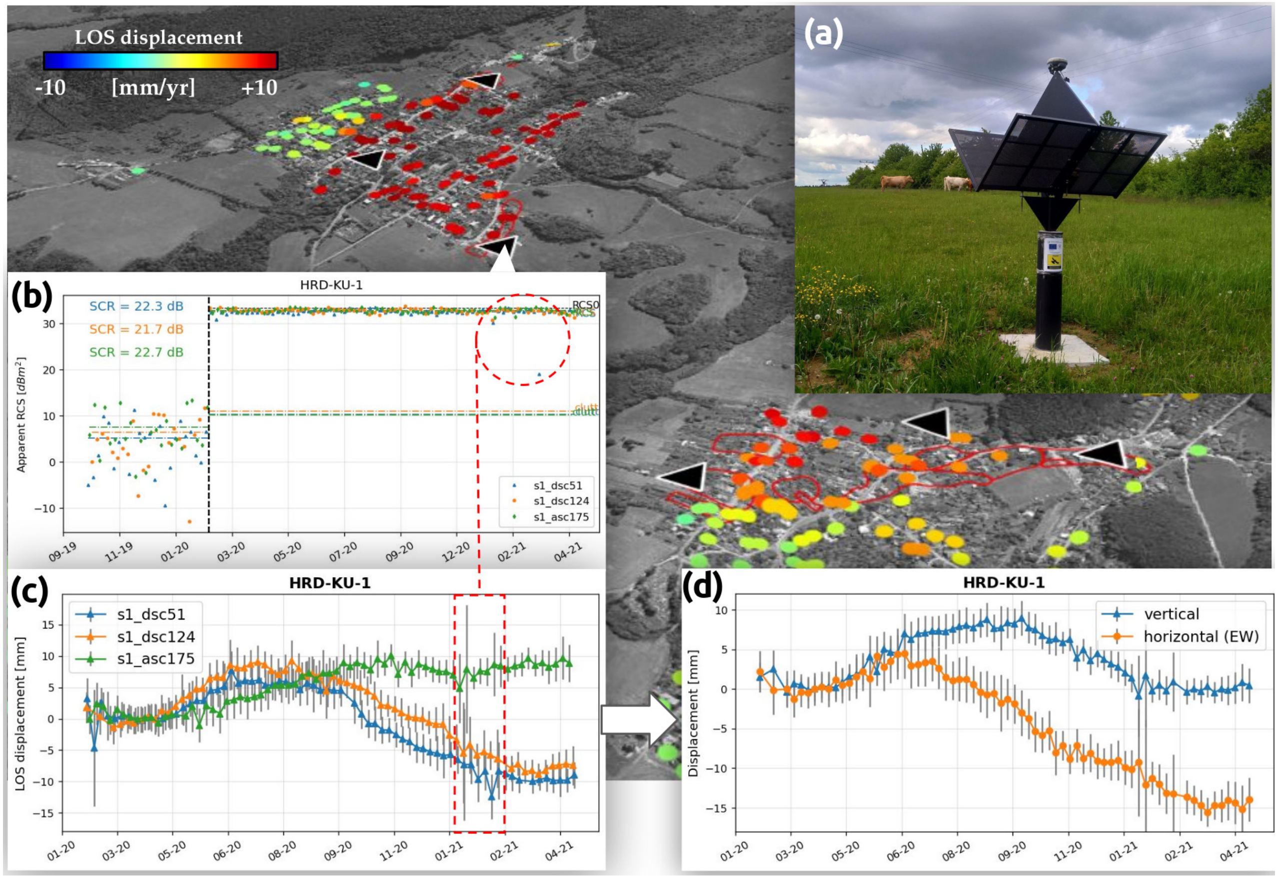

Figure 7: Landslide monitoring at Hradec and Velka Lehotka villages supported by the corner reflectors (a). The time series plots show RCS-based outlier detection (b) and LOS displacement (c) decomposition into vertical and horizontal displacement time series (d).

Table 3: Summary of the Radar Cross Section (RCS), Signal-to-Clutter Ratio (SCR), and Absolute Positioning Error (APE) results for corner reflectors (CR) in The Upper Nitra region.

CR	Sentinel-1 track	RCS [dBm^2] predic.	RCS [dBm^2] estim.	SCR [dB] predic.	SCR [dB] estim.	APE [cm] azimuth	APE [cm] range
HRD-1	ASC175	33.6	32.9 ± 0.3	26.7	24.4	-21 ± 76	-2 ± 16
	DSC51	33.5	32.6 ± 0.3	28.3	24.3	19 ± 50	-8 ± 16
HRD-2	ASC175	33.6	33.1 ± 0.3	25.8	24.0	64 ± 72	-2 ± 14
	DSC51	33.5	32.5 ± 0.4	26.9	22.4	44 ± 56	-12 ± 18
HRD-3	ASC175	33.6	33.2 ± 0.4	19.5	21.0	27 ± 101	9 ± 20
	DSC51	33.5	32.1 ± 0.4	26.5	22.4	10 ± 50	-9 ± 18
LHE-1	ASC175	33.6	33.0 ± 0.3	27.9	24.2	12 ± 57	3 ± 18
	DSC51	33.5	33.0 ± 0.4	24.7	22.2	29 ± 89	-15 ± 20
LHE-2	ASC175	33.6	33.2 ± 0.4	23.1	21.7	31 ± 74	-2 ± 21
	DSC51	33.5	32.8 ± 0.3	28.7	25.1	6 ± 58	-10 ± 16
LHE-3	ASC175	33.6	33.4 ± 0.4	26.3	21.7	-81 ± 81	-28 ± 14
	DSC51	33.5	32.9 ± 0.3	25.4	23.2	-11 ± 77	5 ± 20
LHE-4	ASC175	33.6	33.2 ± 0.3	25.4	23.7	38 ± 66	2 ± 19
	DSC51	33.5	32.8 ± 0.3	24.0	23.6	17 ± 62	-13 ± 17

3 Radar Transponders for InSAR Geodesy

Radar transponders are active electronic devices that receive a radar signal, amplify it, and transmit it back to its source, such as a satellite carrying a SAR antenna. They can serve as a compact alternative to corner reflectors (CR) for precise SAR positioning (Gruber et al. 2020), SAR interferometry (InSAR), deformation monitoring over areas with few natural coherent scatterers (Mahapatra et al. 2014), InSAR datum connection, and geodetic data integration to provide an absolute reference to the inherently relative InSAR measurements (Mahapatra et al. 2017). Recently, medium to low cost transponders for such applications have entered the market for C-band SAR sensors, which triggers questions about their performance and applicability for specific studies. In particular, this concerns their precise radiometric and geometric characteristics, InSAR phase stability, and dependence of external secular or seasonal effects, such as variations in temperature and humidity. Especially for long-term geodetic applications, or as permanent reference stations, there is a need for performance metrics. The aim of this study is to derive these quantitative quality metrics based on multi-year experiments with transponders.

Measuring 360×570×233 mm, they contain two pairs of transmit and receive antennas, for the ascending and descending orbits of right-looking satellites, such as Sentinel-1 and Radarsat-2. The transponder receives the C-band signal via a squinted receive 'patch' antenna, amplifies it, and transmits it back to the source using equally oriented transmit 'patch' antenna. It operates at a bandwidth of 5.405 GHz ± 100 MHz. The antennas are placed under the protective plastic dome, see Fig. 8(a), transparent to C-band signals. Their orientation can be optimized for the average line-of-sight direction at the latitude at which they are deployed. For European latitudes, they are squinted in azimuth by 12° (southward from the east-west direction) and tilted in elevation by 32° with respect to the zenith. The azimuth and elevation beamwidths are 20° and 40°, respectively, enabling an orientation to the average Sentinel-1 incidence and zero-Doppler angles for overlapping tracks, while allowing for slight misalignment. The transponder is switched on automatically based on the selected satellite overpass times. The main function of the integrated GNSS receiver is to keep the internal oscillator of the microcontroller synchronized with respect to the time reference (UTC). With an expected overall RF gain of 50 dB, the expected RCS of the transponders is 44 dBm^2.

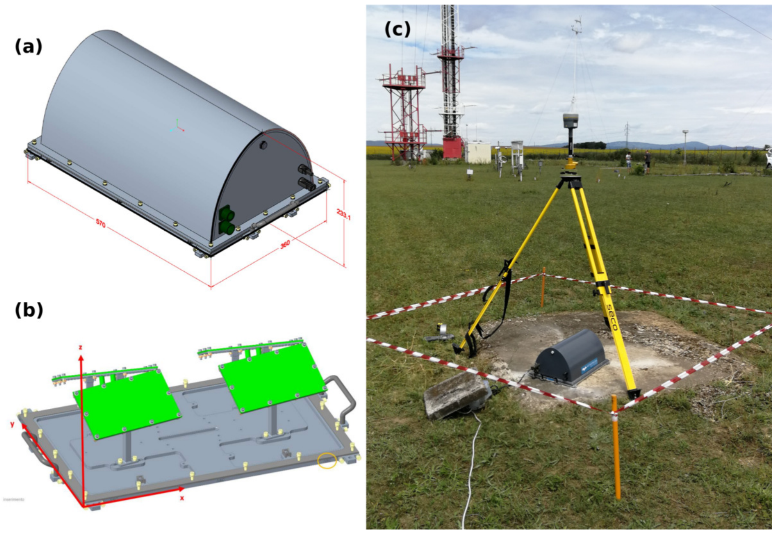

Figure 8: (a) ECR-C model, (b) antennas under radome (Metasensing 2019), (c) ECR141 during static GNSS positioning.

3.1 Experiment setup

The first experiment is performed at the meteorological station in Slovakia, nearby the permanent GNSS station JABO of the SKPOS network, see Fig. 8(c). At this site, we test the performance of two transponders, ECR141 and ECR148, see Table 4, which are in a very short baseline configuration of 46.5 m length. The second experiment is performed at the TU Delft artificial radar reflector test site, WASS, located in Wassenaar, The Netherlands. At this site, we test the performance of two transponders, ECR100 and ECR128, see Table 4. The positions of the transponders were selected such that: (i) it guarantees a high SCR, (ii) avoiding the interference of their impulse response by separating them mutually and from proximate point scatterers. The transponders are fastened on horizontal concrete slabs. At the WASS test site, we use six reference corner reflectors (CRAS, CRDS, and double reflectors DBFT, DBFX, the same as in the experiments in Section 2.1. All reference reflectors are deployed since 2017 and their RCS and phase stability are well known. ECR100 and ECR128 form very short baselines w.r.t. the reference reflectors. The long-term stability of the concrete slabs carrying the transponders has been verified by repeated levelling measurements carried out since 2013. For our experiments, we use meteo data from the nearby meteo stations.

Using GECORIS toolbox, see Section 2.2, we analyzed nearly 1000 Sentinel-1 SLC time series acquired from two overlapping ascending and two overlapping descending tracks covering the transponders. Table 4 summarizes the number of Sentinel-1 data used for the operational period of the tested transponders.

Table 4: Summary of the four tested transponders and Sentinel-1 data used until 28 March 2021

Transponder	Location	Operational since	No. Sentinel-1a+b acquisitions	
			ascending	descending
ECR100	WASS, Wassenaar, Netherlands	2019/06/19	104 + 105	107 + 106
ECR128	WASS, Wassenaar, Netherlands	2020/04/04	56 + 58	58 + 58
ECR141	JABO, Jaslovske Bohunice, Slovakia	2020/07/09	41 + 42	41 + 40
ECR148	JABO, Jaslovske Bohunice, Slovakia	2020/07/09	41 + 42	41 + 40

3.2 Results and Discussion

In the following, we discuss the results of our experiments considering the amplitude behaviour, InSAR phase stability, and absolute positioning in sections 3.2.1–3.2.3, respectively.

3.2.1 Radiometry

Fig. 9 shows an example of the oversampled radar brightness for all reflectors at the WASS test site.

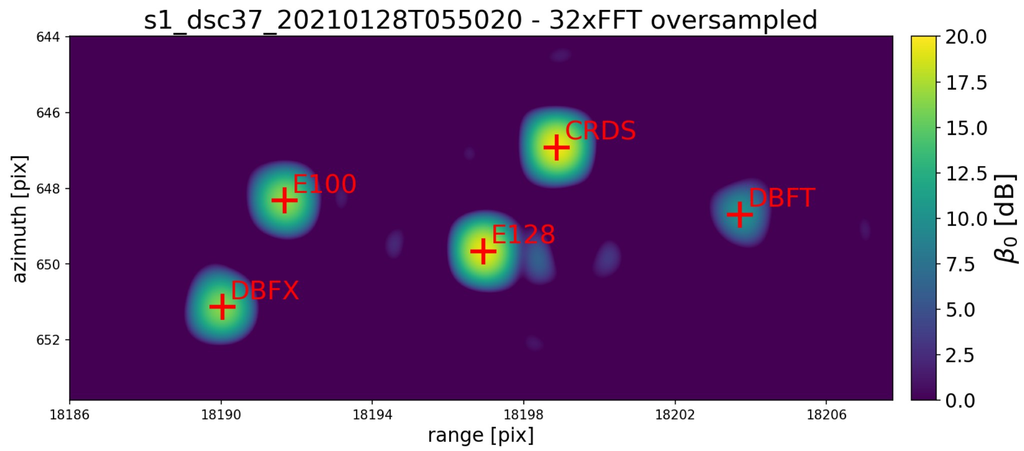

Figure 9: The radar brightness β_0 image patch showing all reflectors at the WASS test site.

The temporal average RCS of the units ECR128, ECR141, and ECR148 ranges from 42 dBm^2 to 45 dBm^2 across Sentinel-1 tracks, while the temporal average RCS of unit ECR100, which is an older prototype, is approximately 4 dB lower. Note that 45 dBm^2 is equivalent to a triangular trihedral corner reflector with leg-length longer than 2.0 m. These values are in agreement with the theoretical value given by formula using gains of the transponder's components (Brunfeldt & Ulaby 1984, Freeman et al. 1990).

The RCS averages differ between tracks, depending on incidence angle and zero-Doppler direction, resulting in antenna misalignment and subsequently RCS attenuation. Fig. 10 shows this average RCS plotted against a misalignment in elevation and azimuth angles.

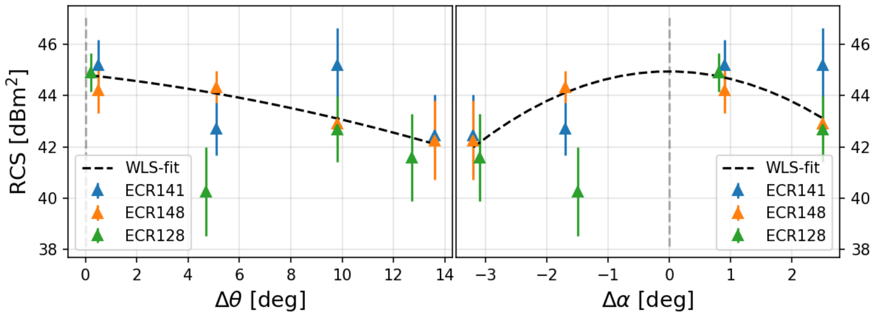

Figure 10: RCS versus antenna misalignment in elevation ($\Delta\theta$) and azimuth ($\Delta\alpha$) angles. A weighted-least-squares fit approximates the attenuation by a quadratic polynomial. Error-bars are 2.5 sigma.

We observe maximally 3 dB RCS loss for 13° and −3° misalignment in elevation and azimuth angles, respectively. Compared to a triangular trihedral corner reflector, an equivalent misalignment would yield an attenuation of ~1.5 dB. Considering a SCR of 20 dB, a 3 dB loss increases the phase error by ~0.1 mm. We approximate the observed attenuation by a quadratic polynomial by a weighted-least-squares (WLS) fit (excluding the data from prototype ECR100 due to its constant offset). The only large residual appears for ECR128, track 37, which could be due to a slightly erroneous antenna orientation within the sealed casing of the transponder.

Comparing the temporal RCS stability of the transponders with conventional corner reflectors, see Table 5, we find that despite the higher average RCS of the transponders, their RCS standard deviations, σ_{RCS}, are significantly higher. For the WASS test site, both the reflectors and the transponders experience identical clutter conditions, which implies that the observed σ_{RCS} is not influenced by the clutter. The temporal RCS stability of the transponders is comparable to the DBFT reflector, which has a more than 10 dB lower RCS. In section 3.2.2 we show the implications of the RCS stability on the temporal phase stability.

Table 5: RCS standard deviations for corner reflectors and transponders, in [dBm^2].

Target	Type	Site	average RCS	σ_{RCS}			
				ASC88	ASC161	DSC37	DSC110
CRAS / CRDS	reflector	WASS	39.0	0.13	0.19	0.14	0.19
DBFX	reflector	WASS	35.4	0.24	0.21	0.16	0.22
DBFT	reflector	WASS	28.6	0.44	0.42	0.47	0.44
ECR100	transponder	WASS	38.4	0.58	0.68	0.46	0.46
ECR128	transponder	WASS	42.4	0.69	0.68	0.51	0.30
ECR141	transponder	JABO	43.9	0.42	0.63	0.58	0.40
ECR148	transponder	JABO	43.4	0.25	0.62	0.35	0.36

For a correct interpretation of transponder time series, it is important to understand whether the RCS is susceptible to systematic temporal variations. Fig. 11 shows scatter plots of transponders' RCS plotted in combination with hourly surface temperatures. The RCS variability of the units in the WASS test site does not show a significant correlation with temperature, and neither does the variability of the descending data of the JABO test site. However, there is a significant correlation of −0.82 for the ascending data of the JABO test site's ECR141. Thus, this temperature dependency is observed (i) in only one of the two test sites (JABO), (ii) in only one of the two viewing geometries (ascending), (iii) for environmental temperatures higher than 20°C, which only occur in the ascending (afternoon) orbits, and (iv) in two independent units (ECR141 and ECR148). This suggests that temperature variations do not necessarily affect the RCS, but if they do, it occurs mainly for temperatures higher than 20°C. An increase in temperature results in a (slight) decrease of RCS for these acquisitions. Note that this would lead to a 1 dBm^2 reduction in RCS, hence, a 1 dB reduction in SCR, which is equivalent to less than 0.2° phase error for an SCR>30.

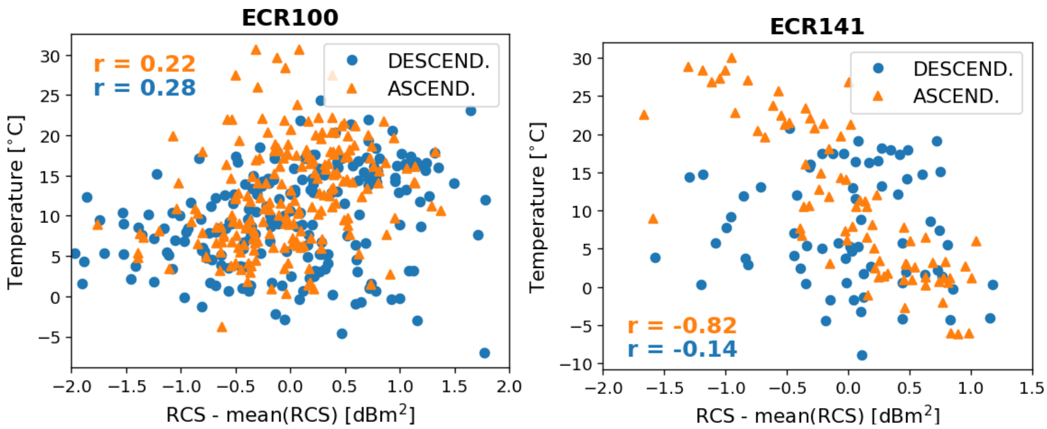

Figure 11: RCS variability versus surface temperature for the two transponders, including Pearson's sample correlation coefficient r.

3.2.2 InSAR Phase Stability

Deploying compact transponders is arguably most interesting for applications that use the phase information, i.e., SAR interferometry. This requires an assessment of the reliability and stability of the transponder phase. At the WASS test site we evaluate this using a configuration that combines transponders and corner reflectors at distances of less than 70 m, which results in an atmospheric differential signal that is on average 0.03 mm (Hanssen 2001), corresponding to 0.4° for C-band, respectively. This allows us to evaluate the temporal coherence, i.e. the phase stability, of the transponders, as the phase variance should be dominated by the clutter, described by the SCR of the transponders, and the sensor's thermal noise.

Flattened and topography-corrected interferograms were computed for all Sentinel-1 stacks, and subsequently interferometric phase time series, evaluated at the IRF peaks, were used to compute double-difference phase time series between transponders and reflectors. Fig. 12 shows double-difference (DD) phase time series between a transponder's ascending oriented antenna and a reference reflector, for all Sentinel-1 tracks. As the seasonal signal is apparent in the time series, we also plot the surface temperature readings of a nearby meteo-station (Voorschoten) obtained for the whole hour closest to the Sentinel-1 acquisition. To verify that this signal is not coming from the reference reflectors, we also compute DD time series between the independent reference reflectors.

Fig. 13 with scatter plots of the LOS displacement against the temperature, measured from the ascending tracks, shows a significant correlation for the transponders, while practically no correlation for CR. While such a seasonal signal could be also caused by the actual displacement between the concrete slabs carrying the reflectors, repeated levelling measurements do not show such displacements. Therefore, the phase measurements of the ECRs are indeed sensitive to the temperature variations, with a typical dependency of 0.07–0.15 mm per °C.

For the transponders at test site JABO, we cannot compute independent phase DD's as there is no nearby reference corner reflector. Therefore, Fig. 14 only shows phase DD's, converted to LOS

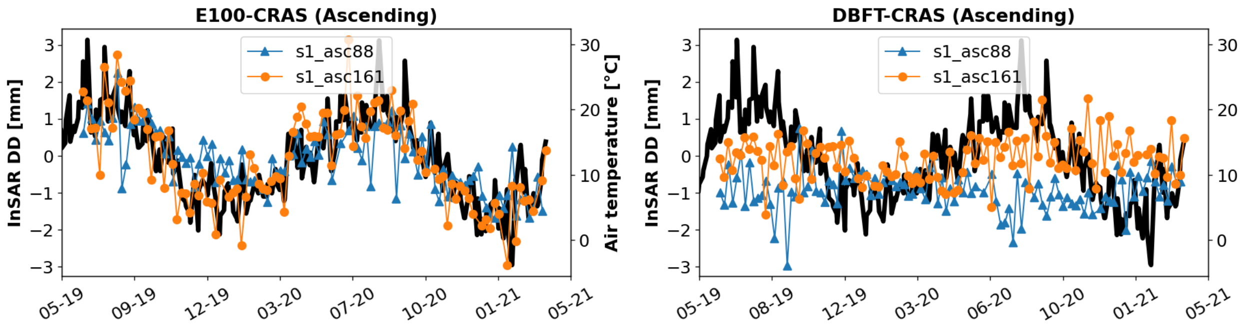

Figure 12: InSAR phase double-difference (DD) for transponder ECR100 and reflector DBFT, relative to a reference corner reflector CRAS, plotted against air temperature for test site WASS.

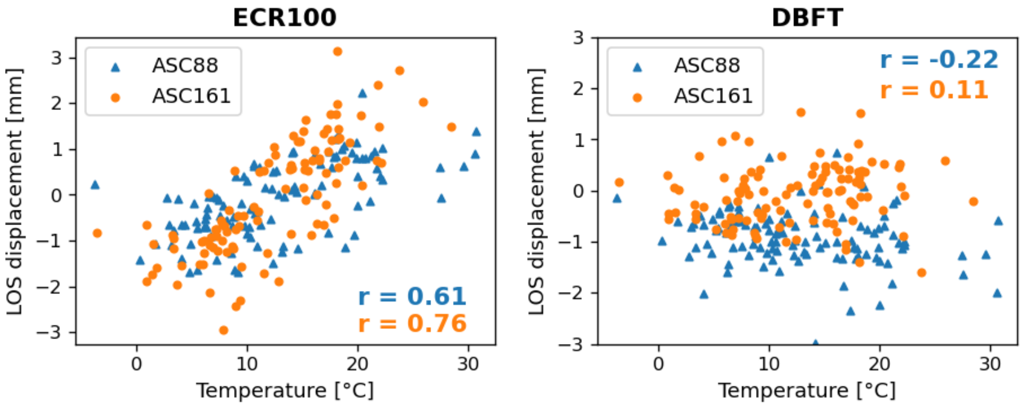

Figure 13: InSAR LOS displacement of transponder E100 and reference reflector DBFT plotted against temperature, for test site WASS.

displacements, over the very short baseline between ECR141 and ECR148. Assuming the same temperature dependency for both the units, it should cancel out over this baseline. However, the residual correlation of the InSAR phases with the surface temperature is apparent. Unfortunately, in this case we cannot rule out actual subsidence or uplift of one of the concrete blocks carrying the transponders. In Fig. 14 we also compare the LOS displacement time series with the snow cover data of test site JABO. The sudden 2 mm phase jumps in January and February of 2021 are clearly a consequence of the snow and ice cover on the transponder's radomes, as shown by the snow cover time series in Fig. 14.

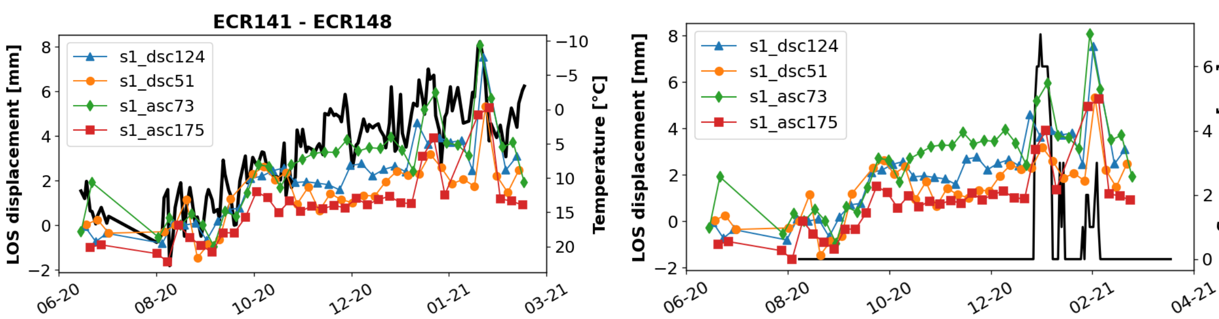

Figure 14: Time series of InSAR phase double-differences (LOS displacement) between ECR141 and ECR148, and surface temperature, and snow cover for test site JABO.

To compensate for the influence of temperature on phase, the transponders would need to have an active temperature control system, such as used by calibration transponders (Raab et al. 2016).

This would, however, increase the complexity, energy consumption, and consequently the cost of the transponders.

In fact, secular and seasonal effects in the time series can be effectively modelled in the post-processing, as long as they remain trend-stationary. Our results show that rather than using a universal equation, each individual transponder requires unique modelling. For each track, we estimate and remove the (seasonal) temperature-dependent signal from the InSAR DD time series assuming the simple linear scaling factor with temperature. The time-dependent trend (drift) is not parameterized, as no displacement trend is observed from the levelling measurements. However, we estimate the drift from the residuals and test its significance using the parameter significance test (Koch 1999). The estimated drift values are reported in Table 6. For ECR100, in track 88-asc and 37-dsc, the estimated drifts are significant (level of significance $\alpha = 0.01$), while neither of the estimated drifts of ECR128 could be proven significant. Since the estimated residual drifts over the baseline between the corner reflectors are not significant, see Fig. 12, we reject the hypothesis that reference reflectors have an influence on the observed drift of the transponders.

After removing the estimated temperature-dependent signal and the residual drift, we assume that the phase residuals are representative of the phase noise and compute the standard deviation (STD) of the residuals. Table 6 shows the estimated STDs for the transponder-reflector (T/R), reflector-reflector (R/R), and transponder-transponder (T/T) baselines before ('raw') and after the trend removal ('detrended'). We compare the estimated STD with the STD predicted using the normalized amplitude dispersion (NAD) (Ferretti et al. 2001) and the temporal average SCR (Dheenathayalan et al. 2017). For the reflectors CRAS and CRDS, we have a reliable estimate of their long-term phase STD, which is $\sigma_{\psi_{CR}} = 0.11$ mm, see Table 1. Therefore, an estimate of the double-difference phase STD for a T/R baseline is obtained by error propagation (assuming uncorrelated measurements). Table 6 shows that the SCR-based estimation of the phase STD gives overly optimistic values, hence the average SCR estimates are biased.

Table 6: InSAR double-difference (DD) phase standard deviation (STD) and drift.

Baseline	Track	InSAR DD phase STD [mm]				Residual drift
		predicted		observed		[mm/yr]
		SCR	NAD	raw	detrended	$\pm 1\sigma$
ECR100 - CRAS	88a	.2	.5	.8	**.5**	-0.5 ± 0.1
	161a	.2	.4	1.2	**.6**	-0.3 ± 0.2
- CRDS	37d	.2	.6	.8	**.6**	-0.4 ± 0.1
	110d	.2	.6	.7	**.6**	-0.3 ± 0.1
ECR128 - CRAS	88a	.2	.3	.9	**.7**	-0.7 ± 0.4
	161a	.2	.5	1.0	**.7**	-0.6 ± 0.3
- CRDS	37d	.2	.6	.6	**.6**	-0.4 ± 0.3
	110d	.2	.6	.5	**.5**	-0.6 ± 0.3
DBFT - CRAS	88a	.4	.4	.5	**.5**	-0.2 ± 0.1
	161a	.4	.4	.6	**.6**	$+0.2 \pm 0.1$
- CRDS	37d	.5	.5	.6	**.6**	0.0 ± 0.1
	110d	.4	.5	.5	**.5**	0.0 ± 0.1

Knowing that the clutter of the transponders has not changed over the monitored period, the assumption of temporal ergodicity fails for the time series of the transponders' peak responses. In other words, the RCS variations are fully displayed in the phase instability. Therefore, the NAD provides a better STD proxy for the transponders. Removing the trend and seasonal components lowers the STDs, cf. Table 6, where the most notable improvement is observed for the ascending tracks, which are more affected by temperature variations. For T/R baselines with ECR100 and ECR128, we observe an average STD of 0.6 mm across all Sentinel-1 tracks.

3.2.3 Absolute Positioning

The positions of the transponder's antenna phase centres (both ascending and descending) in a TRF were determined applying a two-step procedure. First, we determined the coordinates of the transponder reference point, i.e., the northwestern corner of the base-plate, see Fig. 8(b), using GNSS. For the JABO test site, we used static GNSS observations for one hour (with a geodetic-grade receiver Trimble R10), connected to the ETRS89 coordinate reference system (ETRF2000 reference frame) via the nearby permanent reference station JABO (SKPOS network). For the WASS test site, we used four 90-seconds GNSS RTK observations (with a geodetic-grade receiver Trimble R8), connected to the ETRS89 coordinate reference system (ETRF2000 reference frame) using the NETPOS processing service of the Dutch Kadaster. Second, we computed the phase centre coordinates, for each of the antennas, from the reference point coordinates using local coordinate offsets supplied by the manufacturer Metasensing (2019). The accuracy of the TRF coordinates is 1–2 cm in the horizontal and 3 cm in the vertical direction.

The absolute SAR positioning accuracy of the transponders is evaluated by computing the Absolute Positioning Errors (APE) for each acquisition using Eq. (11). Fig. 15a shows APE for the tested transponders and reference reflectors. Observed systematic differences in the range coordinate are primarily caused by the internal electronic delay of the transponders. An approximate internal electronic delay of ~1.5 m (10^{-9} s), including the antennas and protective radome, was estimated by Metasensing (2019). However, the observed average range differences vary between −1.24 m to −2.10 m. Moreover, different internal delays are observed across the individual transponders and between ascending and descending tracks. Fig. 15b shows average range delays plotted against the antenna misalignment in elevation and azimuth angles. We observe nonsystematic shifts between individual transponders. We also observe an apparent shift between ascending (negative $\Delta\alpha$) and descending (positive $\Delta\alpha$) tracks, which is highest for ECR141 (>0.5 m) and smallest for ECR148 (<0.1 m). Although Gruber et al. (2020) report an incidence angle dependence of the transponder's internal range delay, our results could not confirm this. It is interesting to note the completely different range delay behavior between ECR141 and ECR148, despite that these are separated only 46.5 m. For standard deviations of the range coordinate differences, even if the uncertainties of GNSS measurements, orbit state vectors, and atmospheric signal delay corrections are considered, we still reach at least a factor 2 worse results. The average azimuth coordinate differences are all within the confidence interval of their standard deviations. For azimuth standard deviations, we reach the limit dictated by the SCR (CRB) and the azimuth resolution ($\sim 22\ m$).

3.3 Conclusions

From the experimental results with four compact transponders installed at two different test sites, we can draw the main conclusion that each transponder unit is specific in terms of its radiometric, geometric, and phase stability. From the experiments with recent Metasensing ECR-C transponders, we conclude these recommendations:

- Although transponders provide high average RCS, it has significantly higher temporal variations compared to corner reflectors of equivalent RCS. These are unit-specific and may be influenced by environmental temperature variations, mainly for temperatures above 20°C. Therefore, using SCR as the phase precision proxy yields biased estimate.

- Due to the significant antenna-specific internal electronic delays, the transponders might require individual calibration models, similar to the geodetic GNSS antennas, for absolute centimetre-level geodetic positioning purposes.

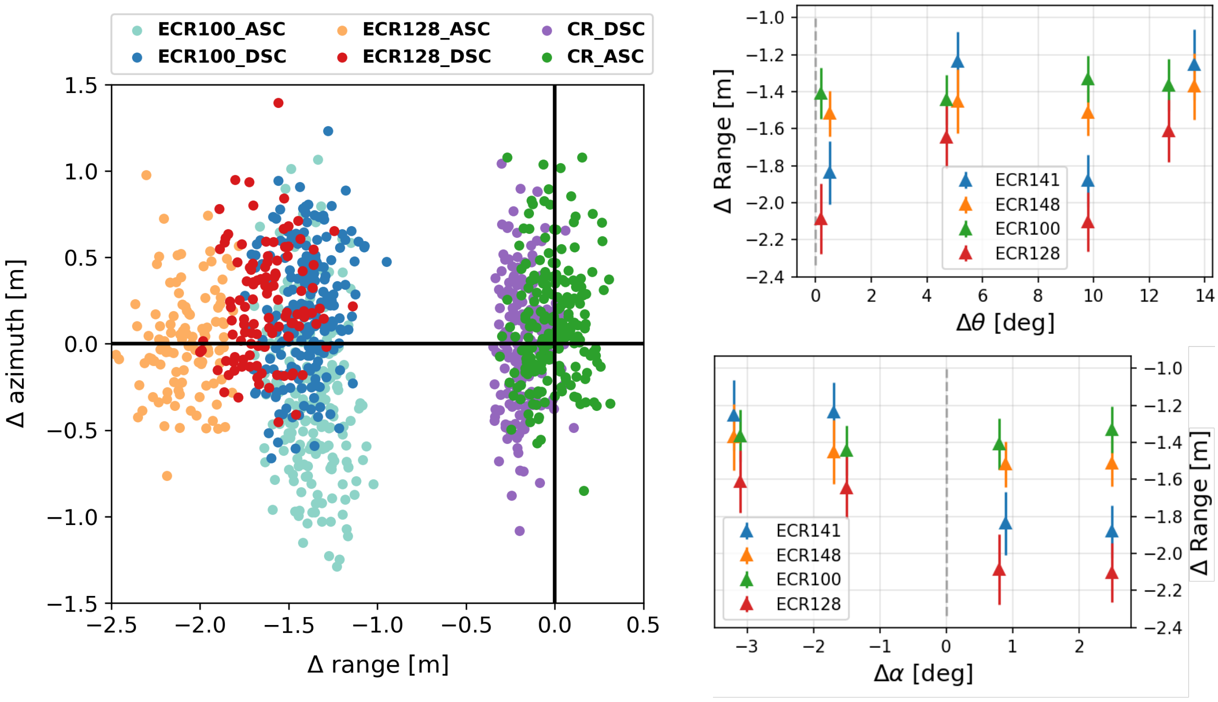

(a)

(b)

Figure 15: Absolute Positioning Errors (APE) on Sentinel-1 data (a) in azimuth and range of the corner reflectors (CRAS/CRDS) and the transponders (ECR100/ECR128) at the WASS test site, (b) in range versus antennas misalignment in elevation ($\Delta\theta$) and azimuth ($\Delta\alpha$) angles. Error-bars are 2.5 sigma.

- The phase measurements of the transponders are sensitive to environmental temperature variations, which can be modelled using simple scaling factor. However, each transponder unit requires a unique modeling.
- The residual phase drift of the transponders is smaller than 1 mm/year, which is especially important for long-term InSAR reliability.
- The observed InSAR phase standard deviations after removing the seasonal trend are within 0.5–1 mm in LOS direction, which is more than factor 2 worse than specified by the manufacturer (Metasensing 2019). Snow or ice cover on the transponder radome causes undesired phase spikes with larger magnitudes than the phase accuracy.

Our main conclusion is that compact radar transponders are a viable alternative to corner reflectors for locations where installation of a corner reflector is not possible or otherwise not practical. However, an individual calibration is recommended for precise InSAR applications, e.g., using transponders as reliable reference points for deformation monitoring. For further research, we recommend repeating the experiments using longer Sentinel-1 and Radarsat-2 SAR time series to obtain a more robust estimate on the InSAR phase stability, especially on the possible secular drift. Moreover, we encourage an intercomparison with the ECR-C units installed within the Baltic height unification initiative (Gruber et al. 2020) or the EUREF initiative.

4 InSAR and GNSS Co-location

In the previous chapters, we have shown the viability of using artificial radar reflectors as phase coherent point scatterers for InSAR geodesy. The particular benefit of artificial reflectors is the precise knowledge of their effective phase centre, allowing their direct co-location with other geodetic measurements in the observation space. The only remaining assumption is that the measurement points of different techniques undergo the same motion in time. To satisfy this assumption, measurement points of different techniques could be rigidly connected within a single instrument, the co-location station. Under such circumstances, co-locating radar reflectors and instruments of absolute space geodetic technique, such as continuous GNSS measurements, allows: (i) to have a reliable network of reference points; (ii) to transform multiple InSAR measurements from different acquisition geometries into a common, well-defined terrestrial reference frame; and (iii) to validate the InSAR measurement quality. Continuously operating reference GNSS stations (CORS), as part of the state-wide permanent GNSS networks, are well-suited to serve as a foundation for integrating InSAR measurements in an absolute geodetic datum.

The advantages/disadvantages of passive/active radar reflectors for geodetic InSAR co-location are summarized in Table 7.

Table 7: Pros and cons of the passive/active radar reflectors for InSAR geodesy and geodetic co-location.

Reflector	passive (corner reflector)	active (transponder)
Complexity	simple, easy to manufacture	relatively complex electronic device
Size	large/bulky (esp. for longer wavelengths)	small/compact
Environmental susceptibility	conspicuous (vandalism), wind-loading, clogging (debris, precipitation)	temperature, snow/ice cover
Maintenance	minimal (clogging)	power supply, GPS clock synchronization, firmware updates
Cost and availability	cheap, various shapes	more expensive, new on commercial market, prototypes
Selectiveness	always on, multiple frequencies/polarizations	selective (e.g., C/X-band, polarization, on-time)
SAR geometry	single (ascending or descending)	multiple
RCS	size-and orientation-dependant, good temporal stability	RF-chain-and orientation-dependant, temporal stability susceptible to temperature
SAR positioning	apex known and easy to measure	antenna phase centre offsets necessary, antenna-specific internal electronic delays
InSAR	phase-stable	phase stability dependant on RF chain, temperature-dependant, possible secular drift
Multi-year reliability	well-verified (possible damage, vandalism)	individual calibration recommended (drift, temperature variations, electronics degradation)
GNSS co-location	only new stations, robust construction required, height separation to avoid GNSS multipath	easy to install also at existing stations, flexible mounting options required for maintenance

Our objective was to design an in-house co-location station within a single monument. For co-location stations using corner reflectors, it is important to minimize the negative influence of corner reflectors on the quality of GNSS signals (multipath), which is the main concern for GNSS network operators. On the other hand, the influence of the station's monument on the radar clutter should be minimal. The requirement was to use the standard GNSS antenna mounting monument used by the SKPOS permanent stations (SKPOS 2021), i.e., a concrete-filled corrugated plastic pipe with 400 mm diameter and an interior steel armature. We combine it with the well-verified DBST reflector design from the landslide monitoring experiences, see Section 2.2. The main advantage of using a back-flipped reflector is avoiding the need to dip them to achieve proper LOS alignment. Hence CR can be connected to the mounting structure with their vertical central plates directly. The principal design question was how to mount the CR on the GNSS antenna pole or pillar. Multipath effects induced by co-located CR were studied in depth by (Fuhrmann et al. 2021). They analyze the influence of two 60 cm square trihedrals attached to the GNSS antenna pole with a vertical distance of 50 cm from the top of the reflectors. Their experiments show that CR have no significant effect on daily GNSS coordinates (less than 0.1 mm), and they induce smaller multipath effects compared to multipath observed at GNSS sites on buildings. Experiments by Kamphuis (2019) show clear quality loss due to multipath when the GNSS antenna is placed directly above the CR, but no negative influence with height separation of > 1.3 m

From the InSAR perspective, the pipe protruding above and below the reflector's central plate causes undesired secondary reflection with a different phase centre as the primary reflection from a corner reflector. This can cause either constructive/destructive interference, possibly diminishing the SCR and jeopardizing the final phase centre position. To find the influence of the pipe on the clutter, we first simulate the RCS of the pipe as a top-hat reflector using geometric optics (Doerry 2008). Considering the shallowest local incidence angle of the Sentinel-1 measurements (44°), the analytical RCS of this 1.3 m high top-hat reflector with 0.4 m diameter is approximately 17 m^2. The RCS of the DBST reflector under such circumstances is >1600 m^2, i.e., almost 100 times stronger. In terms of the SCR, this corresponds to gain or loss of ±0.05 dB, which is one order smaller than the radiometric accuracy of Sentinel-1. To confirm the simulation results, we perform an experiment by mounting an empty corrugated pipe, in the ascending reflector (west one), protruding 1.3 m above the opposite reflector's central plate. For Sentinel-1 descending acquisition, we estimate the RCS and peak position of the opposite reflector's (descending, east) response and compare it to the average RCS and positioning before the pipe was mounted. This experiment confirms the results of the simulation, showing no detectable RCS or positioning changes.

In the final design, the reflectors are mounted 1 m above the ground to minimize undesired ground reflection for CR (Doerry 2008). Therefore, the horizontal reflector plates are >1.3 m below the GNSS antenna. Although squinting the reflectors by ∼12 degrees in azimuth would yield ideal bore-sight alignment with Sentinel-1 measurements, it would also increase the complexity of the carrying construction. Therefore, we have opted for the straightforward east/west orientation of the reflectors, hence connecting them within a single carrying construction of four steel rods drilled through the pipe, filled with concrete. The photo of the built prototype station is in Fig. 16.

The average RCS of both ZVOL reflectors observed from one year of Sentinel-1 time series is in concert with analytical RCS values and comparable to other DBST reflectors in Slovakia. The clutter power is estimated to be at approximately the same level before/after the station installation. Considering the multipath effects in the GNSS signals received by the ZVOL station, GNSS operator SKPOS (2021) reports nominal values comparable to other stations without the corner reflectors.

Finally, we have assessed the co-location suitability of all SKPOS permanent stations. Many of the stations, especially those with GNSS receivers mounted on roofs of buildings, were found to be unsuitable due to high levels of clutter. Considering the limited possibilities to install bulky corner reflectors on already existing stations, radar transponders are a plausible alternative. Our co-location design with corner reflectors (Fig. 16) is preferred for all future SKPOS stations. After sufficient time series of Sentinel-1 measurements are accumulated, the co-location stations will serve as a geodetic reference for InSAR time series analysis at regional, up to nationwide scale Parizzi et al. (2020).

The potential of InSAR geodesy will only grow with future SAR satellite missions. Co-location stations integrating InSAR and GNSS measurements will be essential for the robust validation scheme of the InSAR products from national and international initiatives, such as the European Ground Motion Service (Larsen et al. 2020).

Figure 16: The new type of InSAR and GNSS co-location reference station (ZVOL) of the permanent SKPOS network (SKPOS 2021).

5 Research Contributions

I InSAR theory with the emphasis on geodetic particulars was summarized, addressing the readers from the geodetic community.

II The foundation for the state-of-the-art geodetic InSAR time series software was developed, including the quality control and integration of artificial radar reflectors.

III In-depth study of the radiometric, geometric, and interferometric particulars of analyzing SAR time series of artificial radar reflectors was performed.

IV A new 'temporal method' for estimating the Signal-to-Clutter Ratio (SCR) of InSAR corner reflectors was devised.

V Novel software for analyzing SAR time series of artificial radar reflectors, GECORIS, was developed and provided to the public under a free and open-source license.

VI First corner reflector networks were built for landslide monitoring and geodetic InSAR integration in Slovakia.

VII The viability and reliability of radar transponders as a compact alternative to corner reflectors for InSAR geodesy were tested in multi-year field experiments.

VIII A prototype permanent station for co-location of InSAR and GNSS measurements was designed, built, and tested.

List of Author's Publications

Peer-reviewed Journal Papers

Czikhardt, R., van der Marel, H., Papco, J. "GECORIS: An Open-Source Toolbox for Analyzing Time Series of Corner Reflectors in InSAR Geodesy." *Remote Sensing*. 2021; 13(5):926. ISSN: 2072-4292. DOI: https://doi.org/10.3390/rs13050926

Czikhardt, R., van der Marel, H., van Leijen, F. J., Hanssen, R. F. "Estimating Signal-to-Clutter Ratio of InSAR Corner Reflectors from SAR Time Series." *IEEE Geoscience and Remote Sensing Letters*. 2021; PP(99):1-5. 1558-0571. DOI: https://doi.org/10.1109/LGRS.2021.3070045.
Citations: 1 SCOPUS/WoS

Czikhardt, R., van der Marel, H., Hanssen, R. F. "Multi-year Field Tests of Compact Radar Transponders for InSAR Geodesy." *Manuscript submitted for publication*. 2021.

Bakon, M.; **Czikhardt, R.**; Papco, J.; Barlak, J.; Rovnak, M.; Adamisin, P.; Perissin, D. "remotIO: A Sentinel-1 Multi-Temporal InSAR Infrastructure Monitoring Service with Automatic Updates and Data Mining Capabilities." *Remote Sensing*. 2020; 12:1892. ISSN: 2072-4292. DOI: https://doi.org/10.3390/rs12111892
Citations: 7 SCOPUS/WoS

Czikhardt, R., Papco, J., Bakon, M., Liscak, P., Ondrejka, P., Zlocha, M. "Ground Stability Monitoring of Undermined and Landslide Prone Areas by Means of Sentinel-1 Multi-Temporal InSAR, Case Study from Slovakia", *Geosciences*. 2017; 7(3), 87. ISSN 2076-3263. DOI: https://doi.org/10.3390/geosciences7030087
Citations: 18 SCOPUS/WoS

Peer-reviewed Conference Proceedings

Czikhardt, R. "Testing Metasensing ECR-C geodetic radar transponders." *In Advances in Architectural, Civil and Environmental Engineering*. Bratislava: Spektrum STU, 2020, s. 153–164. ISBN 978-80-227-5052-3.

Czikhardt, R. "Performance assessment of first GNSS-collocated artificial SAR reflector in Slovakia." *In Advances in Architectural, Civil and Environmental Engineering*. Bratislava: Spektrum STU, 2019, s. 106–113. ISBN 978-80-227-4972-5.

Bakon, M., Rovnak, M., **Czikhardt, R**, Papco, J., Admisin, P. "Satellite solution for structural damage monitoring as a tool for sustainable smart cities." *In SGEM 2019. 19th International Multidisciplinary Scientific GeoConference.* Volume 19. Ecology, Economics, Education and Legislation: conference proceedings. Albena, Bulgaria, 30 June - 6 July 2019. 1. vyd. Sofia : STEF 92 Technology, 2019, s. 669–677. ISBN 978-619-7408-84-3.

Czikhardt, R., Papco, J., Bakon, M. "Feasibility of the Sentinel-1 Multi-temporal InSAR system based on the SNAP and StaMPS: Case study from the Tatra Mts., Slovakia." *Procedia Computer Science.* 2018; 138, 366 - 373. ISSN 1877-0509. DOI: https://doi.org/10.1016/j.procs.2018.10.052.

Czikhardt, R. "Atmospheric systematic effects in multi-temporal InSAR and methods to mitigate them." *In Advances in Architectural, Civil and Environmental Engineering:* 28th Annual PhD Student Conference on Applied Mathematics, Applied Mechanics, Building Technology, Geodesy

and Cartography, Landscaping, Theory and Environmental Technology of Buildings, Theory and Structures of Buildings, Theory and Structures of Civil Engineering Works, Water Resources Engineering. 2018. ISBN 978-80-227-4864-3.

Czikhardt, R. "Simulation of geometric distortions in SAR images implemented in MATLAB and published online." *In Proceedings of Student V4 Geoscience conference and scientific meeting GISÁČEK* 2017. Ostrava - Czech Republic: VŠB - Technical University of Ostrava, pp. 112-119. ISBN 978-80-248-4033-8.

Conference Contributions

Czikhardt, R., Papco, J., Ondrejka, P., Ondrus, P., and Liscak, P. "Corner Reflector Network as a Geodetic Reference for Landslide Monitoring via InSAR Time Series: Case Study from Slovakia", *EGU General Assembly 2021*, online, 19–30 Apr 2021, EGU21-12373, https://doi.org/10.5194/egusphere-egu21-12373.

Czikhardt, R., Papčo, J., Bakoň, M. "Sentinel-1 state-wide multi-temporal InSAR processing for recognition of active natural hazards in Slovakia", *ESA Living Planet Symposium 2019*, MiCo - Milano Congressi, Milan - Italy, 13. - 17. May 2019

Czikhardt, R., Papčo, J., Droščák, B., Ferianc, M. (2018). "A pilot study on the Sentinel-1 InSAR surface deformation monitoring system: Tatra Mts., Slovakia", *EUREF Symposium 2018*, Amsterdam - The Netherlands, 30. May - 1. June 2018

Czikhardt, R., Papčo, J. (2017). "Recent surface deformation trends of the Sub-Tatra basin as seen by Sentinel-1 Multi-Temporal InSAR", *16. predvianočný geologický seminár SGS: Nové poznatky o stavbe a vývoji Západných Karpát*, SAV, Bratislava - Slovakia, 7. December 2017

Papčo, J., Bakon, M., **Czikhardt, R.**, Lesko, M. (2017). "Ground Stability Monitoring of the selected sites in Slovakia using InSAR technology", *In Geodesy, Cartography and Geoinformatics 2017*, Demanova dolina, Low Tatras - Slovakia, 10. - 13. October 2017

Czikhardt, R., Papčo, J. (2017). "Ground Stability Monitoring of the Sub-Tatra Basin by Means of Sentinel-1 Multi-Temporal InSAR", *XII. Slovak Geophysical Conference*, Commenius University, Bratislava - Slovakia, 28. - 29. September 2017

Papčo, J., **Czikhardt, R.**, Bakoň, M., Leško, M., Liščák, P., Ondrejka, P. (2017). "Využitie radarovej interferometrie na sledovanie pohybových tendencií geologicky zaujímavých oblastí", *Otvorený geologický kongres Slovenskej geologickej spoločnosti a České geologické společnosti*, Vysoké Tatry - Slovakia, 14. - 17. júna 2017

Bakoň, M., Oliveira, I., Perissin, D., Sousa, J., Papčo, J., Qin, Y., **Czikhardt, R.** (2017). "Data Mining Approach for Multivariate Outlier Detection in Post-Processing of Multi-Temporal InSAR Results: Case Studies", *Poster at Advances in the Science and Applications of SAR Interferometry and Sentinel-1 InSAR*, Aalto University in Helsinki - Finland, 5 - 9 June 2017

References

Adam, N., Parizzi, A., Eineder, M. & Crosetto, M. (2009), 'Practical persistent scatterer processing validation in the course of the Terrafirma project', *Journal of Applied Geophysics* **69**(1), 59–65.

Ansari, H., De Zan, F. & Bamler, R. (2018), 'Efficient phase estimation for interferogram stacks', *IEEE Transactions on Geoscience and Remote Sensing* **56**(7), 4109–4125.

Balss, U. et al. (2018), Survey protocol for geometric sar sensor analysis, Technical report, German Aerospace Center (DLR), Technical University of Munich (TUM), Remote Sensing Laboratories - University of Zurich (RSL).

Bamler, R. & Eineder, M. (2005), 'Accuracy of differential shift estimation by correlation and split-bandwidth interferometry for wideband and delta-k SAR systems', *IEEE Geoscience and Remote Sensing Letters* **2**(2), 151–155.

Bamler, R. & Hartl, P. (1998), 'Synthetic aperture radar interferometry', *Inverse Problems* **14**(4), R1–R54.

Brunfeldt, D. R. & Ulaby, F. T. (1984), 'Active Reflector for Radar Calibration', *IEEE Transactions on Geoscience and Remote Sensing* **GE-22**(2), 165–169.

CLS (2020), Sentinel-1a n-cyclic performance report - 2020-07, Technical Report 7, Collecte Localisation Satellites (CLS), Ramonville Saint-Agne, France.

Crosetto, M., Monserrat, O., Bremmer, C., Hanssen, R., Capes, R. & Marsh, S. (2009), 'Ground motion monitoring using SAR interferometry: quality assessment', *European Geologist Magazine* **26**, 12–15. NEO.

Cumming, I. G. & Wong, F. H. (2005), *Digital processing of Synthetic Aperture Radar data: : Algorithms and Implementation*, Vol. 1, Artech House.

Czikhardt, R., Papco, J., Bakon, M., Liscak, P., Ondrejka, P. & Zlocha, M. (2017), 'Ground stability monitoring of undermined and landslide prone areas by means of sentinel-1 multi-temporal insar, case study from slovakia', *Geosciences* **7**(3).

Czikhardt, R., van der Marel, H. & Papco, J. (2021), 'GECORIS: An Open-Source Toolbox for Analyzing Time Series of Corner Reflectors in InSAR Geodesy', *Remote Sensing* **13**(5).

Czikhardt, R., van der Marel, H., van Leijen, F. J. & Hanssen, R. F. (2021), 'Estimating Signal-to-Clutter Ratio of InSAR Corner Reflectors From SAR Time Series', *IEEE Geoscience and Remote Sensing Letters* **PP**(99), 1–5.

Dainty, J. C., ed. (1975), *Laser Speckle and Related Phenomena*, Vol. 9 of *Topics in Applied Physics*, Springer-Verlag, Heidelberg.

Dheenathayalan, P., Cuenca, M. C., Hoogeboom, P. & Hanssen, R. F. (2017), 'Small reflectors for ground motion monitoring with InSAR', *IEEE Transactions on Geoscience and Remote Sensing* **55**(12), 6703–6712.

Dheenathayalan, P., Small, D., Schubert, A. & Hanssen, R. F. (2016), 'High-precision positioning of radar scatterers', *Journal of Geodesy* **90**(5), 403–422.

Doerry, A. W. (2008), Reflectors for sar performance testing, Technical report, Sandia National Laboratories, Albuquerque, New Mexico 87185 and Livermore, California 94550.

ESA (2021), 'Sentinel application platform (snap)', Available online: https://step.esa.int/main/toolboxes/snap/ (accessed on 22 Februry 2021).

Ferretti, A., Prati, C. & Rocca, F. (2001), 'Permanent Scatterers in SAR Interferometry', *IEEE Transactions on Geoscience and Remote Sensing* **39**(1), 8–20.

Ferretti, A., Savio, G., Barzaghi, R., Borghi, A., Musazzi, S., Novali, F., Prati, C. & Rocca, F. (2007), 'Submillimeter accuracy of InSAR time series: Experimental validation', *IEEE Transactions on Geoscience and Remote Sensing* **45**(5), 1142–1153.

Freeman, A. (1992), 'SAR calibration: An overview', *IEEE Transactions on Geoscience and Remote Sensing* **30**(6), 1107–1121.

Freeman, A., Shen, Y. & Werner, C. L. (1990), 'Polarimetric SAR calibration experiment using active radar calibrators', *IEEE Transactions on Geoscience and Remote Sensing* **28**(2), 224–240.

Fu, W., Guo, H., Tian, Q. & Guo, X. (2010), 'Landslide monitoring by corner reflectors differential interferometry sar', *International Journal of Remote Sensing* **31**(24), 6387–6400.

Fuhrmann, T., Garthwaite, M. C. & McClusky, S. (2021), 'Investigating GNSS multipath effects induced by co-located Radar Corner Reflectors', *Journal of Applied Geodesy* .

Garthwaite, M. C. (2017), 'On the Design of Radar Corner Reflectors for Deformation Monitoring in Multi-Frequency InSAR', *Remote Sensing* **9**(7).

Garthwaite, M. C., Nancarrow, S., Hislop, A., Thankappan, M., Dawson, J. H. & Lawrie, S. (2015b), The design of radar corner reflectors for the australian geophysical observing system: A single design suitable for insar deformation monitoring and sar calibration at multiple microwave frequency bands., Technical report, Geoscience Australia, Canberra.

Gisinger, C., Schubert, A., Breit, H., Garthwaite, M., Balss, U., Willberg, M., Small, D., Eineder, M. & Miranda, N. (2021), 'In-Depth Verification of Sentinel-1 and TerraSAR-X Geolocation Accuracy Using the Australian Corner Reflector Array', *IEEE Transactions on Geoscience and Remote Sensing* **59**(2), 1154–1181.

Gisinger, C., Willberg, M., Balss, U., Klügel, T., Mähler, S., Pail, R. & Eineder, M. (2016), 'Differential geodetic stereo SAR with TerraSAR-X by exploiting small multi-directional radar reflectors', *Journal of Geodesy* **91**.

Gray, A., Vachon, P., Livingstone, C. & Lukowski, T. (1990), 'Synthetic aperture radar calibration using reference reflectors', *IEEE Transactions on Geoscience and Remote Sensing* **28**(3), 374–383.

Groot, J. (1992), 'Letter: Cross section computation of trihedral corner reflectors with the geometrical optics approximation', *European Transactions on Telecommunications* **3**(6), 637–642.

Gruber, T., Ågren, J., Angermann, D., Ellmann, A., Engfeldt, A., Gisinger, C., Jaworski, L., Marila, S., Nastula, J., Nilfouroushan, F., Oikonomidou, X., Poutanen, M., Saari, T., Schlaak, M., Światek, A., Varbla, S. & Zdunek, R. (2020), 'Geodetic SAR for Height System Unification and Sea Level Research—Observation Concept and Preliminary Results in the Baltic Sea', *Remote Sensing* **12**(22).

Guarnieri, A. & Tebaldini, S. (2008), 'On the exploitation of target statistics for SAR interferometry applications', *IEEE Transactions on Geoscience and Remote Sensing* **46**(11), 3436–3443.

Hanssen, R. (2017), 'A radar retroreflector device and a method of preparing a radar retroreflector device'. International Patent WO2018236215A1.
URL: https://patents.google.com/patent/WO2018236215A1/en

Hanssen, R. F. (2001), *Radar interferometry: data interpretation and error analysis*, Vol. 2, Springer Netherlands.

Hanssen, R. F., van Leijen, F. J., van Zwieten, G. J., Dortland, S., Bremmer, C. N. & Kleuskens, M. (2008), Validation of PSI results of Alkmaar and Amsterdam within the Terrafirma validation experiment, *in* 'Fifth International Workshop on ERS/Envisat SAR Interferometry, Frascati, Italy, 2007', p. 6 pp.

Hersbach, H. & Dee, D. (2016), 'Era5 reanalysis is in production', *ECMWF Newsletter* **147**, 5–6.
URL: https://www.ecmwf.int/en/newsletter/147/news/era5-reanalysis-production

IERS (2021), 'International earth rotation and reference systems service', Available online: https://www.iers.org/ (accessed on 22 Februry 2021).

IGS (2021), 'International gnss service', Available online: http://www.igs.org/ (accessed on 22 Februry 2021).

Kampes, B. M. (2006), *Radar Interferometry: Persistent Scatterer Technique*, Springer, Dordrecht, The Netherlands.

Kampes, B. M. & Hanssen, R. F. (2004), 'Ambiguity resolution for permanent scatterer interferometry', *IEEE Transactions on Geoscience and Remote Sensing* **42**(11), 2446–2453.

Kamphuis, J. (2019), Co-location of geodetic reference points, Master's thesis, TU Delft Civil Engineering and Geoscience, Stevinweg 1, 2628 CN Delft, The Netherlands.

Ketelaar, V. B. H. G. (2009), *Satellite Radar Interferometry: Subsidence Monitoring Techniques*, Springer Netherlands.

Koch, K.-R. (1999), *Parameter Estimation and Hypothesis Testing in Linear Models*, 2 edn, Springer-Verlag, New York.

Larsen, Y., Marinkovic, P., Dehls, J., Bredal, M. & C. Bishp, e. a. (2020), European Ground Motion Service: Service Implementation Plan and Product Specification Document, Technical report, European Environment Agency, Kongens Nytorv 6 1050 Copenhagen K Denmark.
URL: https://land.copernicus.eu/user-corner/technical-library/european-ground-motion-service

Mahapatra, P., Samiei-Esfahany, S., van der Marel, H. & Hanssen, R. (2014), 'On the Use of Transponders as Coherent Radar Targets for SAR Interferometry', *IEEE Transactions on Geoscience and Remote Sensing* **52**(3), 1869–1878.

Mahapatra, P., van der Marel, H., van Leijen, F., Samiei Esfahany, S., Klees, R. & Hanssen, R. (2017), 'InSAR datum connection using GNSS-augmented radar transponders', *Journal of Geodesy* .

Marinkovic, P., Ketelaar, V., van Leijen, F. & Hanssen, R. (2008), Insar quality control: Analysis of five years of corner reflector time series, *in* H. Lacoste & L. Ouwehand, eds, 'Fifth International Workshop on ERS/Envisat SAR Interferometry, 'FRINGE07', Frascati, Italy, 26 Nov-30 Nov 2007', ESA Communication Production Office, pp. 1–8. niet eerder opgevoerd.

Metasensing (2019), ‘Metasensing bv: Radar solutions - electronic corner reflector - c band (ecr-c)’, https://www.geomatics.metasensing.com/ecr-c.

Miranda, N. (2017), *Definition of the TOPS SLC deramping function for products generated by the S-1 IPF*, 3 edn, European Space Agency. Reference: COPE-GSEG-EOPG-TN-14-0025.

Miranda, N. & Meadows, P. J. (2015), Radiometric calibration of s-1 level-1 products generated by the s-1 ipf, Technical report, European Space Agency (ESA). ESA-EOPG-CSCOP-TN-0002.

Oliver, C. & Quegan, S. (2004), *Understanding synthetic aperture radar images*, SciTech Publ.

Ondrejka, P., Bakon, M., Papco, J. & Liscak, P. (2016), ‘Monitoring of sliding activity of the territory prievidza-hradec’, *Geotechnika* **1/2016**, 3–12. In Slovak with English summary.

Parizzi, A., Rodriguez Gonzalez, F. & Brcic, R. (2020), ‘A Covariance-Based Approach to Merging InSAR and GNSS Displacement Rate Measurements’, *Remote Sensing* **12**(2).

Peter, H., Jäggi, A., Fernández, J., Escobar, D., Ayuga, F., Arnold, D., Wermuth, M., Hackel, S., Otten, M., Simons, W., Visser, P., Hugentobler, U. & Féménias, P. (2017), ‘Sentinel-1a – first precise orbit determination results’, *Advances in Space Research* **60**(5), 879 – 892.

Piantanida, R., Miranda, N. & Hajduch, G. (2017), Thermal Denoising of Products Generated by the S-1 IPF, Technical report, MPC-S1.

Quin, G. & Loreaux, P. (2013), ‘Submillimeter Accuracy of Multipass Corner Reflector Monitoring by PS Technique’, *IEEE Transactions on Geoscience and Remote Sensing* **51**(3), 1775–1783.

Raab, S., Doering, B. J., Rudolf, D., Reimann, J. & Schwerdt, M. (2016), Analysis of an Improved Temperature Management Concept for SAR System Calibration Transponders, *in* ‘Proceedings of EUSAR 2016: 11th European Conference on Synthetic Aperture Radar’, pp. 1–6.

Raney, R. K., Freeman, T., Hawkins, R. W. & Bamler, R. (1994), A plea for radar brightness, *in* ‘Proc. IEEE International Geoscience and Remote Sensing Symposium (IGARSS ’94)’, Vol. 2, pp. 1090–1092.

Sadeghi, Z., Wright, T., Hooper, A., Jordan, C., Novellino, A., Bateson, L. & Biggs, J. (2021), ‘Benchmarking and inter-comparison of Sentinel-1 InSAR velocities and time series’, *Remote Sensing of Environment* **256**, 112306.

Samiei-Esfahany, S., Martins, J. E., van Leijen, F. & Hanssen, R. F. (2016), ‘Phase Estimation for Distributed Scatterers in InSAR Stacks Using Integer Least Squares Estimation’, *IEEE Transactions on Geoscience and Remote Sensing* **54**(10), 5671–5687.

Schmidt, K., Schwerdt, M., Miranda, N. & Reimann, J. (2020), ‘Radiometric Comparison within the Sentinel-1 SAR Constellation over a Wide Backscatter Range’, *Remote Sensing* **12**(5).

SKPOS (2021), ‘Slovak real time positioning service’, Available online: http://www.skpos.gku.sk/en/ (accessed on 22 Februry 2021).

Small, D. & Schubert, A. (2019), Guide to Sentinel-1 Geocoding, Technical report, Remote Sensing Laboratories - University of Zurich (RSL).

Teunissen, P. J. G. (1993), Least-squares estimation of the integer gps ambiguities: Lrs series 6, Technical report, Delft Geodetic Computing Centre, Delft University of Technology, Delft, The Netherlands.

Teunissen, P. J. G. & Amiri-Simkooei, A. R. (2008), ‘Least-squares variance component estimation’, *Journal of Geodesy* **82**(2), 65–82.

Ulander, L. M. H. (1991), ‘Accuracy of using point targets for SAR calibration’, *IEEE Trans. Aerosp. Electron. Syst.* **27**(1), 139–148.

van Leijen, F. (2014), *Persistent Scatterer Interferometry based on geodetic estimation theory*, Delft University of Technology.

Yague-Martinez, N., De Zan, F. & Prats-Iraola, P. (2017), ‘Coregistration of Interferometric Stacks of Sentinel-1 TOPS Data’, *IEEE Geoscience and Remote Sensing Letters* **14**(7), 1002–1006.

Yang, M., Dheenathayalan, P., López-Dekker, P., van Leijen, F., Liao, M. & Hanssen, R. F. (2020), ‘On the influence of sub-pixel position correction for PS localization accuracy and time series quality’, *ISPRS Journal of Photogrammetry and Remote Sensing* **165**, 98–107.

Yang, M., López-Dekker, P., Dheenathayalan, P., Liao, M. & Hanssen, R. F. (2019), ‘On the value of corner reflectors and surface models in InSAR precise point positioning’, *ISPRS Journal of Photogrammetry and Remote Sensing* **158**, 113–122.